

Inorganic, Organic, and Perovskite Halides with Nanotechnology for High-Light Yield X- and gamma-ray Scintillators

F. Maddalena, L. Tjahjana, A. Z. Xie, S. W. Zeng, H. Wang, P. Coquet, W. Drozdowski, Christophe Dujardin, C. Dang, M. D. Birowosuto

▶ **To cite this version:**

F. Maddalena, L. Tjahjana, A. Z. Xie, S. W. Zeng, H. Wang, et al.. Inorganic, Organic, and Perovskite Halides with Nanotechnology for High-Light Yield X- and gamma-ray Scintillators. Crystals, 2019, 9, pp.88. 10.3390/cryst9020088 . hal-02285858

HAL Id: hal-02285858

https://univ-lyon1.hal.science/hal-02285858

Submitted on 10 Dec 2020

HAL is a multi-disciplinary open access archive for the deposit and dissemination of scientific research documents, whether they are published or not. The documents may come from teaching and research institutions in France or abroad, or from public or private research centers.

L'archive ouverte pluridisciplinaire **HAL**, est destinée au dépôt et à la diffusion de documents scientifiques de niveau recherche, publiés ou non, émanant des établissements d'enseignement et de recherche français ou étrangers, des laboratoires publics ou privés.

crystals

MDPI

Review

Inorganic, Organic, and Perovskite Halides with Nanotechnology for High–Light Yield X- and γ-ray Scintillators

Francesco Maddalena [1,2], Liliana Tjahjana [1,2], Aozhen Xie [1,2,3], Arramel [4], Shuwen Zeng [5], Hong Wang [1,2,*], Philippe Coquet [1,2,6], Winicjusz Drozdowski [7], Christophe Dujardin [8,*] and Cuong Dang [1,2,3,*] and Muhammad Danang Birowosuto [1,*]

1 CINTRA UMI CNRS/NTU/THALES 3288, Research Techno Plaza, 50 Nanyang Drive, Level 6, Border X Block, Singapore 637553, Singapore; francesco.maddalena@ntu.edu.sg (F.M.); ltjahjana@ntu.edu.sg (L.T.); axie004@e.ntu.edu.sg (A.X.); philippe.coquet@iemn.univ-lille1.fr (P.C.)
2 School of Electrical and Electronic Engineering, Nanyang Technological University, 50 Nanyang Avenue, Singapore 639798, Singapore
3 Energy Research Institute @NTU (ERI@N), Nanyang Technological University, Research Techno Plaza, X-Frontier Block, Level 5, 50 Nanyang Drive, Singapore 637553, Singapore
4 Department of Physics, National University of Singapore, 2 Science Drive 3, Singapore 117542, Singapore; phyarr@nus.edu.sg
5 XLIM Research Institute, UMR 7252 CNRS/University of Limoges, 123, avenue Albert Thomas, 87060 Limoges CEDEX, France; shuwen.zeng@unilim.fr
6 Institut d'Electronique, de Microélectronique et de Nanotechnologie (IEMN), CNRS UMR 8520-Université de Lille, 59650 Villeneuve d'Ascq, France
7 Institute of Physics, Faculty of Physics, Astronomy, and Informatics, Nicolaus Copernicus University, Grudziadzka 5, 87-100 Torun, Poland; wind@fizyka.umk.pl
8 Université de Lyon, Université Claude Bernard Lyon 1, CNRS, Institut Lumière Matière UMR 5306, F-69622 Villeurbanne, France
* Correspondence: ewanghong@ntu.edu.sg (H.W.); christophe.dujardin@univ-lyon1.fr (C.D.); hcdang@ntu.edu.sg (C.Dang); mbirowosuto@ntu.edu.sg (M.D.B.); Tel.: +65-6790-6595 (M.D.B.)

Received: 31 December 2018; Accepted: 04 February 2019; Published: 08 February 2019



Abstract: Trends in scintillators that are used in many applications, such as medical imaging, security, oil-logging, high energy physics and non-destructive inspections are reviewed. First, we address traditional inorganic and organic scintillators with respect of limitation in the scintillation light yields and lifetimes. The combination of high–light yield and fast response can be found in Ce^{3+}, Pr^{3+} and Nd^{3+} lanthanide-doped scintillators while the maximum light yield conversion of 100,000 photons/MeV can be found in Eu^{3+} doped SrI_2. However, the fabrication of those lanthanide-doped scintillators is inefficient and expensive as it requires high-temperature furnaces. A self-grown single crystal using solution processes is already introduced in perovskite photovoltaic technology and it can be the key for low-cost scintillators. A novel class of materials in scintillation includes lead halide perovskites. These materials were explored decades ago due to the large X-ray absorption cross section. However, lately lead halide perovskites have become a focus of interest due to recently reported very high photoluminescence quantum yield and light yield conversion at low temperatures. In principle, 150,000–300,000 photons/MeV light yields can be proportional to the small energy bandgap of these materials, which is below 2 eV. Finally, we discuss the extraction efficiency improvements through the fabrication of the nanostructure in scintillators, which can be implemented in perovskite materials. The recent technology involving quantum dots and nanocrystals may also improve light conversion in perovskite scintillators.

Keywords: scintillator; X-ray; γ-ray; inorganic; organic; perovskite

1. Introduction

Excitation of materials with high-energy radiation always gains interests in studying detection, characterization and fundamental exploration [1–3]. X- and γ-ray photons play an important role because their detection is required in various applications. While direct detection of radiation uses a collection of charges, a scintillator is used for indirect detection since the deposited energy is converted to photons. Scintillators are commonly used for medical diagnostics such as radiography [4], mammographic imaging [5], dosimetry [6], computer tomography (CT) [7], gamma cameras [8], positron emission tomography (PET) [9] and novel techniques such as digital tomosynthesis [10] and dual energy imaging [11]. Other applications of scintillators include security radiation detectors, particle detectors, new energy resource exploration, X-ray security, nuclear cameras [12], and gas exploration [13]. In 2016, the inorganic scintillators already occupied the market share estimated at about USD 256 million [14]. Not to mention, there is also a well established research through academic and industrial collaboration, e.g., Crystal Clear Collaboration [8,15].

A scintillator converts the ionizing radiation through the creation of energetic electrons and holes. This interaction with matter will release the radiation energies through a certain number of emitting photons, each of them having an energy close to either the bandgap of the material or the energy gap between the ground and excited states of an activator. The produced photons are detected by a photodetector and converted into electric signals [8,15,16]. There is also another radiation detection technique through direct registration principle, in which the incoming radiation is directly converted into electrical current in a semiconducting material. However, this detection concept is outside the scope of our study.

In this contribution, the state-of-the-art of scintillator technology is reviewed with a particular emphasis on materials. At first, we focus on the concept, application, and material requirements for scintillators. We then discuss the materials for scintillators starting from traditional organic and inorganic scintillators, followed by discussion of all reported novel lanthanide scintillators. Finally, we point out the current trends in novel materials and nanotechnology in the frame of the research in scintillators as well as the recent progresses on perovskite scintillators. Those can be of interest for low-cost detectors or fast timing applications [14].

2. Concept of Scintillators and Applications

Scintillating materials research started in 1885 when W.C. Rontgen discovered X-rays [17] and became very active since the 1950s when photomultiplier tubes were developed [18]. Scintillators are crucial to several areas of science, including the discovery of electrons, α-particles and more recently, the Higgs boson. Up to this day, the scintillation process remains one of the most useful techniques in scientific research, but its applications extend also to many applicative areas spanning from medical imaging, industrial inspection, homeland security, nuclear waste survey to oil drilling exploration. Therefore, research and development of novel scintillating materials is still a very active domain.

A scintillator detector is constituted by two main parts as depicted in Figure 1a: the scintillator and the photodetector. The scintillator is a material that converts high-energy photons, γ-and X-rays, into ultraviolet (UV) or visible (Vis) light. Scintillators are also capable of emitting UV/Vis when excited by charged particles, such as electrons or protons, as well as neutrons [2]. Scintillators can be organic [19,20] or inorganic materials, and more recently, hybrid organic-inorganic crystals, such as hybrid perovskites [21,22], have emerged as a new class of material for potential interest. The photodetector is an electronic device that converts UV/Vis photons into current, and thus, capable of converting the flashes emitted by the scintillator into electronic signals [23]. Photodetectors can be based on different operational principles, such as p-n junctions, photomultiplier tubes (PMT) and complementary metal–oxide–semiconductor (CMOS) detectors. Many photodetectors exist, with each having their own advantages and drawbacks. Pixellated ones are often used for X-ray imaging, while Photomultiplier Tubes (PMT), Si-PM, avalanche photodiodes or hybrid PMT are used in the counting regime for γ-ray detection.

2.1. Mechanism of the Scintillation Process

As a crude description, the scintillation process can be summarized in three main stages, as depicted in Figure 1b: (I) conversion, (II) transport and energy transfer toward the luminescence center, and (III) luminescence [16,24–28]. The first stage, *conversion*, occurs just after the interaction with the ionizing particle or photon. In this stage, the energy of the incoming radiation is absorbed by the scintillator and highly energetic electrons and holes are created in the material. The exact energy absorption mechanism by the scintillator depends on the type and energy of radiation involved, but for X- or γ-photons the absorption is described by the relation $I/I_0 = e^{-\mu d}$, where I_0 and I are the intensities of the incident and transmitted radiation, μ the linear absorption coefficient and d the thickness of the scintillator. In this review we will focus mainly on detection of photons in the X-ray (100 eV < $h\nu$ < 100 keV) and γ-ray (100 keV < $h\nu$ < 10 MeV) spectrum, although detection of charged particles and even neutrons is possible as well. Three types of interactions between radiation and matter relevantly contribute to the energy conversion process in scintillation: *photoelectric absorption* [29], *Compton scattering* [30], and *pair production* ($h\nu$ > 1022 keV) [31]. Due to their different nature, these processes have different absorption coefficients, which depend mainly on the atomic number Z of the atoms in the scintillator crystal and the energy E of the incoming photons. In the photoelectric effect, the photon energy is fully absorbed by a bound electron, usually a core electron in the *K*- or *L*-shell, which is then ejected, ionizing the host atom. The linear absorption coefficient for the photelectric absorption for energies far from the absorption edges is given by $\mu \sim \rho Z^n / E^{3.5}$ [1,29], where n varies between 3 and 4 and ρ is the scintillator density. Hence, increasing the atomic number of an atom, will increase the absorption probability exponentially, favoring the need of heavy atoms in scintillator crystals. At higher energies, Compton scattering also occurs. It corresponds to an inelastic interaction where a photon is scattered by a (weakly) bound electron and part of the photon energy is transferred to the electron and that deposited energy depends on the scattering angle. Hence, in Compton scattering, the energy deposition is of different energy than the incident radiation. The energy lost by the photon is gained by the scattering electron, which is excited to a higher energy level. The linear absorption coefficient for Compton scattering is given by $\mu \sim \rho / \sqrt{E}$ [1,30]. The absorption in Compton scattering is thus, independent of the atomic number of the atoms present in the crystal and more dependent on the density of the material itself. Finally, if the photon energy is higher than ~1.02 MeV, i.e., higher than twice the rest-mass energy of the electron, pair production is also possible. Pair production is the relativistic phenomenon where the kinetic energy of a particle is converted into new particles and their anti-particles. When sufficiently energetic photons interact with the scintillator crystal the energy of the photon can be converted into an electron-positron pair. The absorption coefficient for pair production is given by $\mu \sim \rho Z ln(\frac{2E}{m_e c^2})$ where $m_e c^2$ is the rest-mass energy of the electron [31]. The overall absorption coefficient scales linearly with the atomic number of the atoms in the material. In addition, unlike the photoelectric effect and Compton scattering, this process becomes more probable as the energy of the photon increases, hence, pair production becomes the dominant interaction at energies above ~8 MeV, generating cascades of secondary particles [8]. As a summary, the energy absorbed by the scintillator crystal will lead to the production of *hot electrons* and *deep holes*, i.e., highly energetic charge carriers, within the scintillator crystal [27]. The hot electrons present in the material will further interact with other particles and pseudo-particles in the solids (electron, plasmon, phonon) within the lattice of the scintillator, leading to an avalanche event of secondary electron–hole pairs. This process will continue until the hot electrons and all the secondary electrons and holes have lost sufficient energy and unable to ionize the ions in the lattice any further. The resulting large number of energetic charge carriers will then undergo energy dissipation through interactions with phonons, so called thermalization. The timescale for the conversion step, including energy absorption and energy dissipation has been estimated to be in the order of 1 ps [8,27]. The holes relax through Auger process and X-ray fluorescence. Charged particles and neutrons, although not discussed here, also lead to the formation of highly energetic charge carriers in the material, and the next two steps in the scintillation process remain almost unchanged, with the exception of the spatial distribution of the interactions.

The second stage of scintillation, *transport and energy transfer*, involves, as the name suggests, the transport of the charge carrier towards the luminescence centers. It is probably the most critical for losses, trapping and timing performances. In this phase, the large number of electrons and holes generated during conversion, migrates through the material. During this stage, several mechanisms can contribute to both delay of the radiative recombination events or loss of efficiency by non-radiative recombination processes and several different models have been proposed in the literature [28]. The origin of these losses is mainly caused by the presence of defects in the scintillator crystal, usually arising from ionic vacancies, ions in interstitial positions, grain boundaries, substitutional impurities or interfacial and surface states. In addition to the intrinsic defects, the interaction of the scintillator crystal with radiation also leads to the formation of further defects, usually Frenkel defects, which are formed when an ion is knocked out of its lattice position into an interstitial space, leaving a vacancy behind [32,33]. The migrating charge carriers can be trapped in these defects, mainly in the vacancies, creating a variety of trap states. Depending on the temperature, trapped electrons and holes can still however be released and migrate further, through phonon-aided hopping transport [34]. Electrons and holes might also move from the delocalized conduction bands into more energetically favorable localized levels by electron/hole-phonon coupling, giving rise to slower moving polarons. It is important to note that the transport phase of scintillation is strongly affected by the fabrication process of the scintillator material [35]. Optimization of crystal growth procedures and material morphology can significantly decrease the number of defects and traps within a material and improve charge carrier mobility and, hence, greatly reduce the non-radiative losses and luminescence delay. For organic, non-crystalline, liquid or vapor scintillators the mechanisms of transport can be even more complex and usually the same models for inorganic crystals do not apply to organic or non-solid scintillators.

In the last stage of scintillation, *luminescence*, the electron and hole are captured through several potential paths by the luminescent center (often an impurity ion in the lattice), promoting it to an excited state. It then recombines radiatively according to the selection rules, emitting light in the UV/Vis spectrum. The physics of luminescent centers and emission is usually well understood [36]. For a fast emission, it is important to select emitting center showing electric dipole allowed transitions, such as the widely used $4f^{n-1}5d \rightarrow 4f^{n}$ transitions in some rare earth metals. Otherwise, if no allowed transition is possible, the charge carriers will need to undergo further processes, leading to slower fluorescence emission, which is a disadvantage for applications requiring fast timing. Hence, in addition to the considerations made for the previous two stages of scintillation, the ions or molecules in the scintillator crystals must be selected such that they will allow for efficient radiative recombination, and a fast decay time when required by the targeted application. Note, this description remains rather crude because such an approach should produce a scintillator exhibiting a proportional response while they almost always are non-proportional. Indeed, spatial distribution of excitation plays a major role through several quenching phenomena during the relaxation stage [37]. Finally, the UV/Vis photons emitted by the scintillator are finally detected by the photodetector, which will convert them into electrical signals.

The overall efficiency of a scintillator detector depends on the shape of the detector itself, the *geometric efficiency*, and the *intrinsic efficiency*, defined as the ratio between the number of photons counted by the detector and the total number of incident photons. The mean number of quanta produced inside the scintillator, i.e., the theoretical light yield, depends on the bandgap of the material and is further discussed in Section 2.3. The actual efficiency of a scintillator depends also on the shape and thickness of the scintillator layer and losses mechanisms, such as self-absorption which causes part of the emitted photons to be absorbed again by the scintillator [38–40]. The geometry can greatly influence phenomena of internal reflection, scattering, and waveguiding within the scintillator, which result in less photons reaching the photodetector. The losses due to this phenomenon can be mitigated by reducing the thickness of the material and optimizing the shape of the scintillator detector.

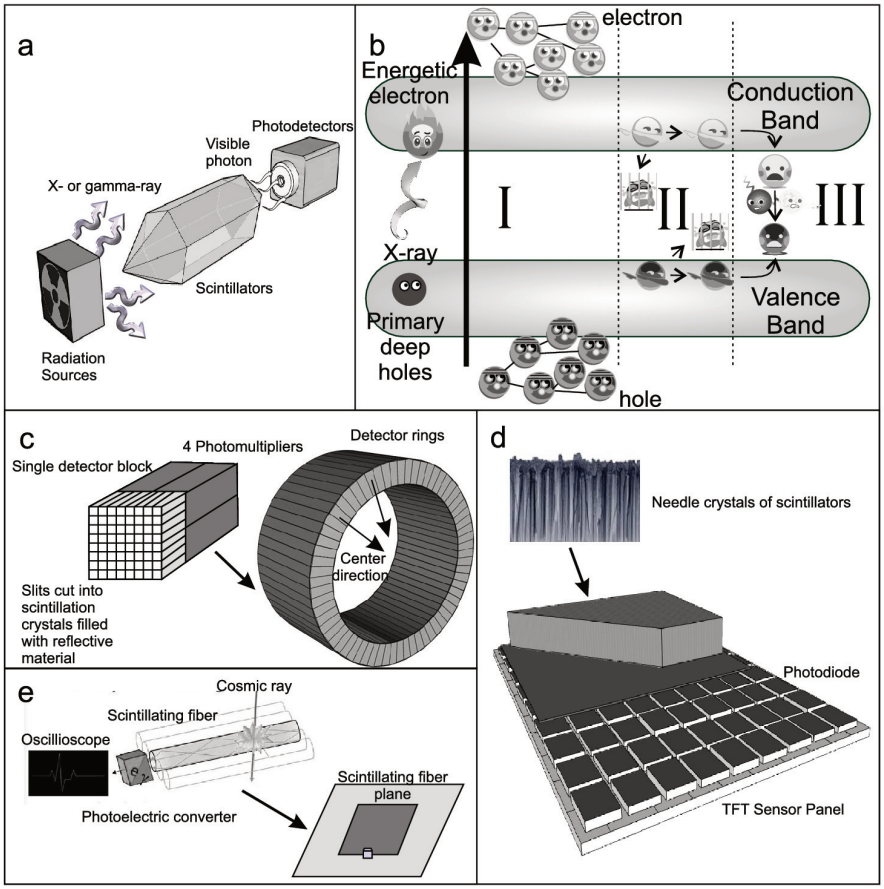


Figure 1. Construction, process, and applications of scintillators: (**a**) A scintillation detector with the main constituent parts. (**b**) A sketch of the scintillator process in crystal. The process is divided into three consecutive stages of (I) conversion, (II) transport and (III) luminescence, which are described in the text. (**c**) Schematic of a detector block and ring of scintillators in a positron emission tomography scanner. (**d**) Needle crystal scintillators used in X-ray digital flat panel detectors (from https://www.trixell.com). (**e**) Scintillating fibers for cosmic-ray detection and high-energy physics experiments.

2.2. Applications of Scintillators

As described above, scintillation is one of the most important technologies, having a vast range of applications across many different fields, such as medical radiography diagnostics, high resolution imaging for scientific and industrial applications, security purposes and high energy physics and astrophysics. Some of the most important applications of scintillators will be discussed below.

Medical diagnostics rely heavily on imaging techniques based on scintillators, such as computed tomography (CT), single-photon emission computerized tomography (SPECT), radiography, mammography, and positron emission tomography (PET). In CT, the patient is irradiated from different directions with X-rays (up to 140 keV) to produce cross-sectional images which can later can be reconstructed into full 3D images. In CT, the scintillators detect the transmitted X-rays, while in PET, the scintillators detect the γ-rays produced by electron-positron annihilation in the patient. These techniques make use of detectors blocks arranged in a circular pattern around the patient as shown schematically in Figure 1c. The detector blocks are made of inorganic scintillator crystals, such as bismuth germanate ($Bi_4Ge_3O_{12}$) [41], cerium-doped lutetium oxyorthosilicate ($Lu_2SiO_5 : Ce^{3+}$) [42] or LYSO, cerium-doped lutetium yttrium orthosilicate ($Lu_{1.8}Y_{0.2}SiO_5 : Ce^{3+}$), positioned in front of photomultiplier tubes. The scintillator crystals are divided into (square) rods and separated by highly reflective material, acting as pixels for the detector block [9] as shown in the insert of Figure 1c. Behind the scintillator the photomultiplier will receive the UV/Vis photons emitted and convert

them into electrical signals. Another example is the familiar X-ray radiography used to detect bone fractures, tuberculosis scarring and dental problems. These techniques are very similar to conventional photography. In fact, radiographic film coupled with a scintillating screen, generally terbium-doped gadolinium oxysulfide ($Gd_2O_2S:Tb^{3+}$) [43], has been the standard system in static radiography for many decades. In recent years, however, driven by the digitalization of the medical field, this more conventional technique has been replaced by flat panel detectors such as the one shown in Figure 1d. The panels are fabricated using thallium-doped cesium iodide ($CsI:Tl$) scintillator as needles, coupled with pixelated silicon photodetectors [44–47], which increases the scintillator thickness and thus, the X-ray absorption efficiency while preserving the spatial resolution. This allows for an improved image quality and increase dose efficiency in order to reduce the patient exposure. In addition, based on similar principles, scintillator detectors with CMOS technology have recently been fabricated and have shown improved radiation resistance of the back-panel detector and improved resolution due to smaller pixel size [48,49].

Although CT and X-ray radiography are often associated with medical applications, their use also extends into the fields of academic research, industrial applications, and security. CT has been extensively used as a non-destructive technique to measure the 3D size and spatial distribution of (rare) samples, such as fossils or meteorites in paleontological and astronomical research respectively. In the industry CT and X-ray radiography are used to study and individuate structural defects, (micro-)fractures, porosity and other material features. X-ray imaging and CT have been also one of the main security features in airports since the early 1970s, particularly in the scanning of luggage or packages for the detection of weapons, explosive devices or certain dangerous substances and goods.

Scintillators not only allow us to do medical imaging and help homeland security, but are also used in particle physics and astrophysics. In experiments performed at particle accelerators such as the Large Hadron Collider at CERN, collisions between protons (or other particles) travelling at relativistic speeds produce a vast number of particles, sometimes with energies in the hundreds of GeV. The particles are measured in detectors called calorimeters. Highly energetic photons are also produced by the collision or as a result of particle decay or interaction between particle and detector screens. Scintillators are used in homogenous calorimeters made of stolzite ($PbWO_4$) in the Compact Muon Sollenoid experiment (CMS) [3] to detect γ-photons or charged particles, providing with high detection efficiency for a wide range of energies [2]. In astrophysics, detection of X-ray and γ-rays is crucial for the investigation of many astronomical phenomena, such as neutron stars, supernova remnants and black holes. Scintillators have been widely used in X-ray and γ-ray telescopes [50]. Scintillators are employed in the detection of cosmic rays as well [51]. Scintillating fiber planes coupled with a photodetectors are also used as schematically depicted in Figure 1e. In the detection mechanism the fiber interacts with the cosmic rays [52], and acts also as a waveguide for the photons produced during the scintillation process, guiding them to the photodetector. For another fundamental application, scintillators are also being used to study neutrinos [53] and rare events such as double β-decay [54].

2.3. Material Requirements for Scintillators

The choice of scintillator material hinges on the practical application requirements. There are several parameters that determine the choice of a particular scintillator [8]:

- *Radiation absorption efficiency, absorption coefficient or absorption length:* This parameter determines how efficiently a material will absorb the radiation during the conversion stage of scintillation. For X-ray and *gamma*-ray detection, materials with high density and high atomic number are preferred as discussed in Section 2.1. A related concept, applied to particle radiation rather than photons, is *stopping power*, which is a measure of how efficiently a material can absorb the kinetic energy of a particle.
- *Light yield (LY):* the number of photons emitted per unit of deposited energy. This is one of the most important parameters of scintillators, playing a major role in determining the scintillators' efficiency, sensitivity, and energy resolution. The light yield depends on by the number of

electron–hole pairs that can be created in the ionization tracks resulting from the interaction of the incident photon and the scintillating material. The number of electron–hole pairs and thus, the light yield are related to the bandgap E_g of the compound [26]. The light yield, expressed in photons/MeV, is given by the relation: $LY = 10^6 \cdot SQ/(\beta E_g)$, where S is the efficiency of electron–hole transport to the optical center, Q is the is the luminescence quantum efficiency of the optical center and β is a constant, usually with a value of ~2.5. Once the light is produced, some losses also occur during the transport to the detector, depending on internal scattering and re-absorption, hence, the actual light yield of a scintillator might be lower than the theoretically expected value, depending also on the geometry of the scintillator.

- *Response time*: the length of time for the scintillator to emit a UV/Vis photon after radiation absorption. The response time is mainly determined by the *decay time* τ of the scintillation. Fast response times, hence, short decay times, are very important for applications where timing is involved such as computer tomography or particle detection in accelerators. However, additional trapping process prior the luminescence in some scintillators, i.e., afterglow, is a disadvantage for this application. Some quenching processes may accelerate the decay as well, but at the cost of the light yield.
- *Self-absorption of light*: For the scintillator, the optical transmission for the nominal thickness for the scintillation spectrum should be considered. If there is too much self-absorption, the converted photons will be reabsorbed and can be lost through non-radiative processes.
- *Energy resolution:* the ratio of the full width at half maximum (FWHM) of the peak at a certain energy in response to the exciting radiation, divided by the peak energy position in the pulse height spectrum. This feature is mainly important for spectral measurements of the incoming radiation, in particular for applications in γ-ray spectroscopy, and the ability of the scintillator to discriminated between different radiation energies. The intrinsic resolution of a scintillator is mainly determined by the non-proportional response of the material, but imperfections such as inhomogeneities in the scintillator resulting into local variations in light output and non-uniform reflectivity can also affect the energy resolution.
- *Emission wavelength:* A spectrum emitted by the scintillator after being excited by the radiation should match the spectrum of the photo-detector, in order to avoid post-scintillation losses. This is called *spectral matching* and is often more of an engineering rather than a material problem, requiring that the sensitivity and efficiency of the detector is near its peak in the spectral region where the scintillator emits. However, materials might need to be tailored in order to conform their emission to available commercial detectors.
- *Stability:* This is divided into chemical and radiation stability. Chemical stability pertains to the intrinsic stability of the material, including self-life. Radiation stability, also called radiation hardness, pertains the ability of the material not to degrade significantly when exposed to radiation. The stability determines thus, how long a material can be used as a scintillator before it needs to be changed.
- *Proportionality:* The scintillation response should be linear with the incident radiation, which can affect intensity discrimination. Although nowadays with computational method it is possible to correct a non-linear response with relative ease, it is still preferable in many occasions to have a linear response of the scintillator, at least in the energy range of interest.

Further important parameters for image resolution which depend on the interaction between scintillator and photodetector rather than the material properties alone are:

- *Spatial resolution*: The parameter is usually known as a modulation transfer function (MTF). This is the spatial frequency response of an imaging system or a component. It is the contrast at a given spatial frequency relative to low frequencies and it is involved in the conversion of contrast values of different-sized objects (object contrast) into contrast intensity levels in the image (image

contrast). The value is relevant to the effective resolution, which accounts for the amounts of blur and contrast over a range of spatial frequencies.

- *Imaging performance*: This is usually the detective quantum efficiency (DQE). Unlike MTF, it is the combined effects of the signal (related to image contrast) and noise performance of an imaging system, generally expressed as a function of spatial frequency. The effective of X-ray imaging for producing an image with high signal-to-noise ratio relative to an ideal detector.

Each of these parameters, and in particular light yield, stability and absorption efficiency, need to be taken into account and prioritized when choosing a scintillator for a particular application and during the search for new materials for scintillation applications.

3. Traditional Scintillators

Scintillating materials have been applied for more than a century starting with Crookes' spinthariscope [18,55]. They can be divided into two classes: inorganic crystalline scintillators, and organic scintillators. While the first class of materials is composed usually of high-density crystals or vapors, the second class of materials are often low-density amorphous solids, or even liquids. Although the main stages of scintillation and radiation absorption processes remain fundamentally the same for all types of scintillators, the exact mechanisms of charge transport, in particular, and luminescence are strongly dependent on the composition morphology of the scintillator. In this section, we will discuss the traditional inorganic and organic scintillators, the materials that have been used widely for the applications and have been around since the discovery of X- and gamma-rays until more than thirty years ago. For inorganic, the most widely used scintillators are thallium-doped sodium iodide ($NaI{:}Tl^+$) and $CsI{:}Tl^+$ and they were discovered about seventy years ago [56]. Organic scintillators were discovered a few years later with Anthracene and plastic scintillators being among the first ones [57].

3.1. Traditional Inorganic Scintillators

Inorganic scintillators are predominantly ionic solids and they are usually grown in high temperature furnaces. Some scintillators have a small amount of activator impurities and among the impurities are thallium (Tl^+), sodium (Na^+), telluride (Te^{2+}), silver (Ag^+), divalent rare earth, and trivalent rare earth ions. For more complete review, a list of some traditional inorganic scintillators is given in Table 1, while a few inorganic scintillators are shown in Figure 2a. Often small amounts of dopant are added to these crystals as *activator*. For example thallium is used to activate sodium iodide in the $NaI{:}Tl^+$ scintillator. Activators create special sites in the lattice of the scintillator crystals, adding localized energy levels generally lying in the bandgap of the crystal. Activators are used either to improve the light yield, quench the afterglow, or modify the emission wavelength. Doping or co-doping ions can act either as luminescent center, but also as traps to modify the transport and energy transfer processes to decrease the afterglow or/and the rise time [58–60].

The earliest scintillator materials, which appeared at the beginning of the 20th century were *scheelite* ($CaWO_4$) and zinc sulfide (ZnS) [2]. These phosphor materials were among the very first to show the property of scintillation when irradiated and were the first to find a practical application, for example in Crookes' ZnS spinthariscope, and still do to this day for a limited number of applications. Using silver as activator, $ZnS{:}Ag^+$ is the scintillator with the one of the highest light yields and a relatively fast response time. However, the overall effective atomic number Z_{eff} of $ZnS{:}Ag^+$ is relatively low, making its absorption efficiency relatively low, hence, forcing the scintillator crystals to be quite thick to be effective but being detrimental for imaging purposes. $CaWO_4$ has found recent applications in the field of particle astrophysics, due to its good energy resolution and high–light yield in particular when exposed to γ-rays [61].

The first single crystal scintillators, $NaI{:}Tl^+$ [62] and $CsI{:}Tl^+$ [63] appeared in the late forties. Figure 2b shows the energy spectrum of the γ-rays emitted by a ^{137}Cs source and measured with a $CsI{:}Tl^+$ coupled with a multi-pixel photon counter (MPPC) array, giving an energy resolution of the

material of about 7% at 662 keV. The scintillation decay curve of $NaI{:}Tl^+$ excited by 662 keV photons from a ^{137}Cs source is shown in Figure 2c giving an average emission lifetime of 230 nanoseconds (ns). As the Figures and Table 1 show, these materials have good light yield, energy resolution and relatively fast response time, which is suitable to be used in the counting regime. In addition the production cost of these materials is relatively low because of their low melting points, hence, $NaI{:}Tl^+$ and $CsI{:}Tl^+$ have fundamentally dominated the scintillation field for more than seventy years.

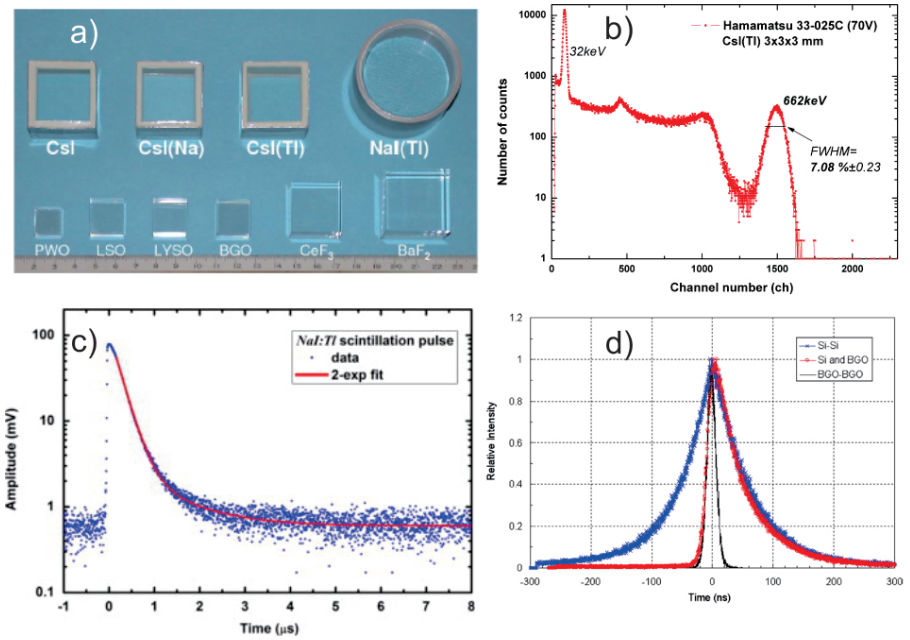


Figure 2. Inorganic and organic traditional scintillators: (**a**) A photo showing traditional scintillators. (**b**) Energy spectrum of 662 keV gamma rays from a ^{137}Cs source, as measured with $CsI{:}Tl^+$ crystals $3 \times 3 \times 3$ mm^3. (**c**) Scintillation decay curve recorded for $NaI{:}Tl$ irradiated with a ^{137}Cs source. Two exponential terms fit to the data is presented with solid line. (**d**) Coincidence timing spectra (timing resolution) from only two silicon detectors (82 nanoseconds (ns) FWHM), $Bi_4Ge_3O_{12}$ (BGO) detectors on the opposite sides (19.4 ns FWHM), and a silicon and BGO detectors on one side of the experimental setup using a ^{18}F source. Figures reproduced from (**a**) Mao, R. et al., *IEEE Nucl. Sci. Symp. Conf. Rec.* **2007**, N49-1, 2285–2291. 2007 by IEEE; (**b**) Grodzicka, M. et al., *J. Inst.* **2013**, 8, P02017. 2013 by IOP Publishing; (**c**) Swiderski, L. et al., *Nucl. Instrum. Methods Phys. Res. A* **2014**, 749, 68–73. 2014 by Elsevier; (**d**) Park, S.-J. et al., *Phys. Med. Biol.* **2007**, 52, 2807–2826. 2007 by IOP Publishing.

Oxides, and in particular $Bi_4Ge_3O_{12}$ (BGO), are also widely used as scintillators. It was first used in the L3 calorimeter in CERN and is still used in PET [3]. Although light yield of BGO is not as high as the light yield of sodium and cesium iodide, it has a very high density and Z_{eff}, making it a very efficient absorber with an excellent photoelectric efficiency, crucial for the sensitivity of PET. Figure 2d compares the timing spectra of two silicon and two BGO detectors using a ^{18}F positron source, showing a much better timing resolution for the BGO detectors in comparison to that of silicon detectors, making them more suitable for applications such as PET-scans operating in coincidence regime. In addition, BGO is also mechanically strong, it is not hygroscopic and has high radiation stability, making it one of the most stable and reliable scintillators on the market. Other widely used inorganic scintillators are shown in Table 1. These, however, generally do not possess a very high yield and/or fast response time compared to $NaI{:}Tl^+$, $CsI{:}Tl^+$ and BGO. Although they are some lanthanide based oxide scintillators that are commonly used in the same applications and sometime can be categorized as traditional scintillator, we decide to discuss them later together with the lanthanide scintillators.

Table 1. Overview of some traditional inorganic scintillators for X-ray and γ-ray detections. The abbreviations in the heading denote the density (ρ), the effective atomic number (Z_{eff}), the emission wavelength (λ) and the main scintillation decay time (τ).

Scintillator	ρ (g/cm^3)	Z_{eff}	Light Yield (photons/MeV)	Energy Resolution (%, at 662keV)	λ (nm)	τ (ns)	Refs.
$NaI{:}Tl^+$	3.7	50.8	43,000	6.7	415	230	[64,65]
$CsI{:}Tl^+$	4.5	54.0	66,000	6.6	560	1000	[64,65]
$CsI{:}Na^+$	4.5	54.0	43,000	7.4	425	-	[65]
CsF	4.6	53.2	1900	19	390	2–4	[66]
BaF_2	4.9	52.7	1430	10	175	0.8	[67]
$CaWO_4$	6.1	75.6	15,800	6.3	425	6800	[61]
$PbWO_4$	8.3	75.6	140	-	~475	~10	[68]
$CdWO_4$	7.9	64.2	19,700	6.5	495	104	[69]
$Bi_4Ge_3O_{12}$	7.1	75.2	8200	27	505	300	[70]
$CdS{:}Te^{2+}$	4.8	48.0	17,000	14	640	270–3000	[71]
$ZnS{:}Ag^+$	4.1	27.4	73,000	-	450	105	[72]

3.2. Traditional Organic Scintillators

Organic scintillators are conjugated hydrocarbon compounds, which feature an extended conjugated system of π-electrons in the double carbon bonds of the molecule. Most commonly, scintillators are aromatic molecules featuring benzene ring structures, such as *Anthracene*. Conjugated systems usually have a smaller band-gap compared to non-conjugated organic molecules, and thus, can produce to strong colors (e.g., indigo dye) and photoluminescence in the visible with a high quantum efficiency, i.e., the number of photons emitted per absorbed photons of the excitation source [73]. Organic scintillators can exist both as solid crystals, as plastics, or as liquid solutions, and can be very durable. The main advantages of organic scintillators over inorganic scintillators, are their inexpensive production cost, often requiring usually low processing temperatures compared to their inorganic counterparts. Optical absorption and emission can be easily tuned through chemical substitution of side groups, which can allow for facile customization of the scintillator. They also often show a rather fast decay time, in the order of a few ns. However, properties such as light yield, energy resolution and absorption efficiency are generally less interesting than those in inorganic crystals. The most common organic scintillators with their properties are listed in Table 2. The highest light yield is shown for *Anthracene* (16,000 photons/MeV), which is often used as benchmark for organic scintillators, is still below most values in Table 1. The smaller X- and gamma-ray absorption lengths than those of inorganic scintillators can be indicated by the low ρ and Z_{eff}. The best energy resolution at 662 keV of 13% for organic scintillators was reported for *Anthracene* as well [57] but most organic scintillators show much worse resolutions due to anisotropic conversion and therefore, we do not put them in Table 2 [74]. In addition, solid crystalline organic scintillators cannot be grown in large sizes, limiting thus, their use. Except for the low production costs, the main advantages is a more efficient and faster detection of thermal neutrons, [75] with the effective neutron/gamma discrimination based on pulse shape as well as pulse height analysis [76].

Table 2. Overview of some organic scintillators. Beside energy resolution, the same convention as in Table 1 is used.

Scintillator	Type	ρ (g/cm^3)	Z_{eff}	Light Yield (photons/MeV)	λ (nm)	τ (ns)	Refs.
Anthracene	Organic crystal	1.25	5.24	16,000	447	30	[57,74]
Stilbene	Organic crystal	1.16	5.14	8000	410	4.5	[74,77]
Naphthalene	Organic crystal	0.96	5.18	2000	348	80	[78]
2,5-*Diphenyloxazole*	Organic crystal	1.06	5.52	8800	405	7	[79]
p-Terphenyl	Liquid Solution	-	-	~9200	440	5	[74]

4. Lanthanide Doped Scintillators

Lanthanide-doped scintillators are mostly inorganic materials. Unlike the traditional one with the activator impurity of Tl^+, we will discuss scintillators with impurities from the rare earth metal ions. Rare earth metals have two types of transitions: spin-allowed $5d \rightarrow 4f$ and spin-forbidden $4f \rightarrow 4f$ transitions. The $5d \rightarrow 4f$ spin-allowed transition may yield to ns lifetimes, which can be useful for application in the counting regime requiring fast response. This emission can be much faster compared to thallium doped traditional scintillators, e.g., 15 ns in $LaBr_3$:Ce^{3+} compared to 1000 ns in CsI:Tl^+. Unlike spin-allowed transitions, the $4f \rightarrow 4f$ spin-forbidden transition is very slow with millisecond (ms) lifetimes. However, because of the lack of non-radiative recombination, the quantum efficiency can be very high almost unity. It is also known for its fundamental advantages such as upconversion, downconversion, and quantum cutting [80,81].

In this section we will restrict the discussion to fast emitters such as: trivalent (Ce^{3+}, Pr^{3+}, and Nd^{3+}) and divalent (Eu^{2+} and Yb^{2+}) lanthanides. Although there are other scintillators with $4f \rightarrow 4f$ forbidden transition of lanthanides, such as Lu_2O_3:Eu^{3+} [82] and Gd_2O_2S:Tb^{3+} (GOS:Tb) [43] powders of X-ray intensifying screen, here we will not focus on these materials since they have usually very long lifetimes, up to ms, making them often unsuitable for many practical applications operating in the counting regime.

4.1. Ce^{3+}, Pr^{3+}, and Nd^{3+} Doped Scintillators

There is a very large variety of trivalent lanthanide-doped scintillators, some of which are listed in Table 3. The $5d \rightarrow 4f$ energy transitions of Ce^{3+}, Pr^{3+}, and Nd^{3+}, which are the most efficient trivalent lanthanide dopants to date, are shown in Figure 3a. Cerium-doped scintillators in particular have shown very high–light yield values and excellent energy resolution [83].

Lutetium based compounds activated with trivalent rare-earth metal ions are also very attractive scintillators, in particular for their high density and effective atomic number. Lutetium-based compounds often show good luminescence properties when doped with Ce^{3+}. Lutetium oxides in general, show good scintillation properties as shown in Table 3. Ce^{3+}- and Pr^{3+}-activated $LuAlO_3$, lutetium aluminum perovskite, has shown a high–light yield for γ-rays (11,400 photons/MeV) and high decay speed of scintillation pulse (17 ns), acceptable energy resolution (23% at 662 keV) and virtually no afterglow emissions and has been considered one of the possible candidates to replace BGO in positron emission tomography [84,85]. In addition, $LuAlO_3$ single crystals have relative high density compared to most scintillators (8.3 g/cm^3), and have a high Z_eff (64.9), making it a particularly effective absorber of X- and γ-rays. They are nevertheless difficult to produced. Lutetium aluminum garnet, $Lu_3Al_5O_{12}$, single crystal scintillators, depicted in Figure 3b for the cerium-activated variant, have also shown also to have high–light yield (∼12,000–19,000 photons/MeV) and fast decay times (∼20–70 ns). Currently high quality $Lu_3Al_5O_{12}$ crystals as well as some other garnets, are commercially available and very promising for industrial applications. Note that bandgap engineering of some garnets have lead to a strong reduction of the afterglow [59]. It also appear recently that co-doping garnet with Mg^{2+} converts a fraction of the Ce^{3+} into the Ce^{4+}. Despite Ce^{4+} is optically non active, it becomes active under ionizing radiation excitation, due to the sequential charge trapping in the transfer process [14]. Another important class of lutetium scintillators, are lutetium orthosilicates, $LuSiO_5$, and lutetium yttrium orthosilicates, $Lu_xY_{2-x}SiO_5$. These show very high–light yields compared to $Lu_3Al_5O_{12}$ and $LuAlO_3$ scintillators, and significantly higher compared to most traditional scintillators, as shown in Figure 3c. The light yields of $LuSiO_5$ and $Lu_xY_{2-x}SiO_5$ are the order 30,000 photons/MeV and show a relatively fast decay time, in the order of 20–40 ns. Like the previous classes of lutetium scintillators, also $LuSiO_5$ and $Lu_xY_{2-x}SiO_5$ scintillators are now available as commercial scintillators.

Ce^{3+}-activated lanthanum halides, $LaCl_3$:Ce^{3+} and $LaBr_3$:Ce^{3+}, have shown a combination of high–light yield, fast response and excellent energy resolution. $LaCl_3$:Ce^{3+} has a light output of 49,000 photons/MeV and an energy resolution of 3.1 % at 662 keV. $LaBr_3$ has even higher light output of 60,000–70,000 photons/MeV for both Ce^{3+}- and Pr^{3+}-activated samples. The energy

resolution $LaBr_3:Ce^{3+}$ is in the order of 2.8 % at 662 keV while the best energy resolution of 2.0 % is reported for $LaBr_3:Ce^{3+}$ with Sr^{2+} and Ca^{2+} co-doping, as seen in Figure 3d [86]. Lanthanum iodide, $LaI_3:Ce^{3+}$, does not show any light yield at room temperature (RT). This scintillator demonstrated its failure due to a too small bandgap of 3.3 eV compared with the 2.9 eV energy difference between the 4f and 5d Ce^{3+} levels [87]. $LuI_3:Ce^{3+}$ has a bandgap of 4.5 eV and this is slightly larger than $LaI_3:Ce^{3+}$ [88]. As a result, it shows a record-breaking light yield for Ce^{3+}-doped scintillators of 98,000 photons/MeV at 662 keV and RT, as shown in Figure 3e [89]. It also has a 33-ns fast response and reasonable good energy resolution, comparable to those of the lanthanum bromide and chloride [89,90]. However, $LuI_3:Ce^{3+}$, like all lutetium-based scintillators has a main drawback due to the intrinsic radioactivity of ^{176}Lu-isotope, a β^--emitter [84]. Although ^{176}Lu is only 2.6% of the totally naturally occurring lutetium and has an extremely long decay time (>37 billion years), it still poses as a possible source of interference, in particular for positron emission tomography applications. In order to counter the interference caused by lutetium radioactive isotopes, the National Electrical Manufacturers Association (NEMA) has recently implemented updated protocols in order to measure the side effect of lutetium natural radioactivity on PET scanner performance and calibrate PET scanners that implement lutetium-based scintillators [91].

Finally, yttrium aluminum perovskite, $YAlO_3$, and yttrium aluminum garnet, $Y_3Al_5O_{12}$, are worth mentioning. These materials feature good light yield, around 17,000 photons/MeV and fast decay times, around 20–30 ns. However, as shown in Figure 3e, they are not as efficient and thermally stable as $LuAlO_3$ or $Lu_3Al_5O_{12}$ scintillators and have an overall lower density and effective atomic number, making them less effective X- and γ-ray absorbers compared to lutetium-based scintillators.

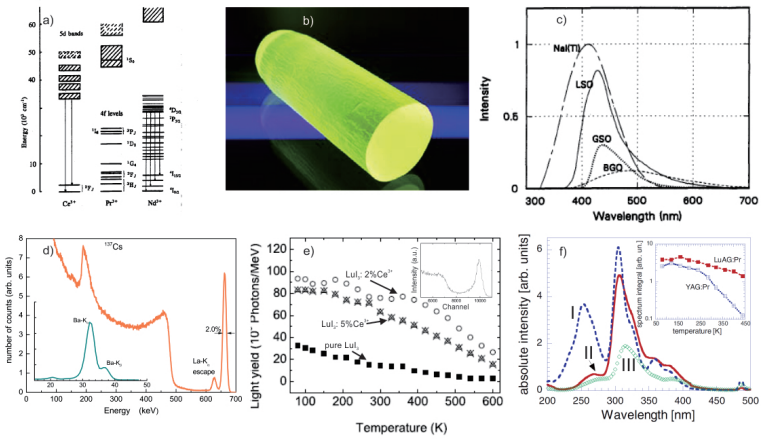


Figure 3. Trivalent lanthanide-doped scintillators: (**a**) Schematic of 4f levels and 5d bands of Ce^{3+}, Pr^{3+} and Nd^{3+} ions in a host lattice. (**b**) Polished cut of $Lu_3Al_5O_{12}:Ce^{3+}$, cerium-doped lutetium aluminum garnet, single crystal under UV lamp excitation. (**c**) Comparison of the γ-ray excited emission spectra (^{241}Am) of $LuSiO_5:Ce^{3+}$ to those of other scintillators. (**d**) The improvement of energy resolution in pulse height spectrum of a ^{137}Cs source measured with a Sr^{2+} codoped $LaBr_3$:5% Ce^{3+} crystal. (**e**) Temperature dependence of the light yields of undoped LuI_3, LuI_3:2%, and 5% Ce^{3+}. The inset shows the pulse height spectra of LuI_3:0.5% Ce^{3+} under ^{137}Cs γ-ray excitation at room temperature (RT). (**f**) X-ray excited emission spectra of $LuAlO_3$: Pr^{3+} (curve (I) at 80 K and (II) at 286 K) and $Y_3Al_5O_{12}:Pr^{3+}$ (curve (III) at 286 K). Spectra are mutually comparable in an absolute way. In the inset, the integral of the spectra within 200–450 nm is given for all temperatures. Figures reproduced from (**a**) van Eijk, C. W. E. et al., *IEEE Trans. Nucl. Sci.* **1994**, 41, 738–741. 1994 by IEEE; (**b**) Nikl, M. et al., *Prog. Cryst. Growth & Charact.* **2013**, 59, 47–72. 2013 by Elsevier; (**c**) Mercher, C.L. et al., *IEEE Trans. Nucl. Sci.* **1992**, 39, 502–505. 1992 by IEEE; (**d**) Alekhin, M.S. et al., *Appl. Phys. Lett* **2013**, 102, 161915-1–161915-4. 2013 by AIP Publishing; (**e**) Birowosuto, M. D. et al., *IEEE Trans. Nucl. Sci.* **2005**, 52, 1114–1117. 2005 by IEEE; (**f**) Nikl, M. et al., *Phys. Stat. Sol. A* **2005**, 202, R4-R6. 2005 by Wiley.

Table 3. Overview of some Ce^{3+}, Pr^{3+}, and Nd^{3+}-doped inorganic scintillators. The same convention as in Table 1 is used.

Scintillator	ρ (g/cm^3)	Z_{eff}	Light Yield (photons/MeV)	Energy Resolution (%, at 662 keV)	λ (nm)	τ (ns)	Ref.
$LaF_3:Ce^{3+}$	5.9	40.3	2200	-	290	3 and 27	[92]
$LaF_3:Nd^{3+}$	5.9	40.3	2000	-	173	6	[93]
CeF_3	6.2	41.1	4500	-	330	28	[92]
$LuF_3:Ce^{3+}$	8.3	50.2	8000	-	310	28	[83]
$K_2YF_5:Pr^{3+}$	3.1	23.9	6900	-	240	20	[94]
$LaCl_3:Ce^{3+}$	3.9	49.5	49,000	3.3	330	25	[95]
$PrCl_3:Ce^{3+}$	4.0	51.5	21,000	8.4	340	17	[96]
$CeCl_3$	3.9	50.4	28,000	-	360	25	[97]
$Cs_2LiLaCl_6:Ce^{3+}$	3.3	41.4	35,000	3.4	400	1 and 40	[98]
$Cs_2LiYCl_6:Ce^{3+}$	3.3	38.1	21,000	6.0	376	1 and 35	[99]
$Cs_2LiYCl_6:Pr^{3+}$	3.3	38.1	10,000	15.0	315	1 and 35	[100]
$K_2LaCl_5:Ce^{3+}$	2.9	44.1	30,000	5.1	344	1000	[101]
$RbGd_2Cl_7:Ce^{3+}$	3.7	53.9	40,000	5.0	370	90	[102]
$LaBr_3:Ce^{3+}$	5.1	46.9	67,000	2.8	358	15	[103]
$LaBr_3:Pr^{3+}$	5.1	46.9	75,000	3.2	450 to 900	11,000	[104]
$PrBr_3:Ce^{3+}$	5.3	48.3	21,000	5.5	365	6	[96]
$GdBr_3:Ce^{3+}$	4.6	52.4	44,000	-	350	20	[105]
$Cs_3LaBr_6:Ce^{3+}$	4.6	42.7	10,400	30.0	390	46	[106]
$Cs_2NaLaBr_6:Ce^{3+}$	3.9	46.9	17,000	11.3	414	61	[107]
$Cs_2NaYBr_6:Ce^{3+}$	3.9	44.5	9500	6.3	420	61	[107]
$Cs_2NaLuBr_6:Ce^{3+}$	4.3	52.3	5800	10.5	422	61	[107]
$Cs_2LiLaBr_6:Ce^{3+}$	3.3	44.1	60,000	2.9	410	55	[98]
$Cs_2LiYBr_6:Ce^{3+}$	4.1	41.5	24,000	7.0	389	85	[99]
$K_2LaBr_5:Ce^{3+}$	3.9	42.8	40,000	4.9	359	100	[108]
$Rb_2LiLaBr_6:Ce^{3+}$	3.9	42.1	33,000	4.8	363	26	[109]
$Rb_2LiYBr_6:Ce^{3+}$	3.8	35.9	23,000	4.7	385	42	[109]
$RbGd_2Br_7:Ce^{3+}$	4.8	50.6	56,000	3.8	420	43	[102]
$K_2LaI_5:Ce^{3+}$	4.4	52.4	57,000	4.2	401	24	[108]
$GdI_3:Ce^{3+}$	5.2	56.9	47,000	4.7	525	45	[110]
$Cs_3Gd_2I_9:Ce^{3+}$	4.7	57.0	2600	-	571	-	[106]
$LuI_3:Ce^{3+}$	5.7	60.5	98,000	4.6	475	33	[89]
$Cs_3LuI_6:Ce^{3+}$	4.8	57.0	1500	-	429	-	[106]
$Cs_3Lu_2I_9:Ce^{3+}$	4.8	57.9	22,800	9.0	556	18	[106]
$Gd_2O_2S:Pr^{3+},Ce^{3+}$	7.3	61.1	40,000	-	511	3000	[111]
$YAl_2O_3:Ce^{3+}$	5.4	25.6	17,000	5.7	370	26	[112]
$Y_3Al_5O_{12}:Ce^{3+}$	4.6	35.1	17,000	3.5	550	85	[113]
$Y_3Al_5O_{12}:Pr^{3+}$	4.6	35.1	16,000	-	300 to 400	18	[114]
$LuAlO_3:Ce^{3+}$	8.3	64.9	11,400	23	365	17	[84]
$Lu_2SiO_5:Ce^{3+}$	7.4	50.2	30,000	10	420	40	[42]
$Lu_2SiO_5:Pr^{3+}$	7.4	50.2	2200	-	247	26	[115]
$Lu_2Si_2O_7:Ce^{3+}$	6.2	46.4	26,000	9.5	378	38	[116]
$Lu_{2.25}Y_{0.75}Al_5O_{12}:Pr^{3+}$	6.2	44.1	33,000	4.4	-	-	[117]
$Lu_3Al_5O_{12}:Ce^{3+}$	6.7	44.3	12,500	-	510	70	[118]
$Lu_3Al_5O_{12}:Pr^{3+}$	6.7	44.3	19,000	4.6	310	20	[119]
$Gd_2SiO_5:Ce^{3+}$	6.7	45.3	12,500	7.0	430	56	[120]
$Gd_2Si_2O_7:Ce^{3+}$	5.5	41.8	40,000	6.0	372	46	[121]
$Lu_{2x}Gd_{2-2x}SiO_5:Ce^{3+}$	7.3	~63	30,000 to 39,000	~8	410 to 430	30 to 40	[122]

4.2. Eu^{2+} and Yb^{2+} Doped Scintillators

In addition to trivalent lanthanides, rare earth elements can also exist in divalent state as well. These lanthanide ions, in particular Eu, and Yb, have been used as dopant in various scintillator crystals. The 4f^n energy level scheme of the free divalent lanthanides is shown in Figure 4a, while Figure 4b,c show singlet $5d \rightarrow 4f$ allowed transition of Eu^{2+} and Yb^{2+}, respectively. Although this is dipole-allowed transition, the $5d \rightarrow 4f$ transition of Eu^{2+} and Yb^{2+} is around ten times slower than that of Ce^{3+}.

Usually, divalent lanthanides are used to dope crystals of group II alkaline metals such as barium, strontium and calcium. The first class of these materials are barium halides, BaX_2, where $X = F, Cl, Br, I$, or mixed halides, i.e., the crystal contains a mixture of different halogen ions. The emission of X-ray excited luminescence spectra of undoped and Eu^{2+}-doped BaX_2 is shown in Figure 4d, and the pulse height spectrum of a ^{137}Cs source measured with undoped and Eu^{2+}-doped $BaBr_2$ crystals and the scintillation decay curves for Eu^{2+}-doped $BaX_2, X = Cl, Br$ are shown in Figure 4e,f, respectively. As seen from Table 4, Eu^{2+}-doped BaX_2 show relatively high–light yield, in particular $BaBrI$, having an light yield of 97,000 photons/MeV, and have a decay time of hundreds of ns, usually less than 600 ns. Other barium-based scintillators, like barium phosphates, barium orthosilicates and barium oxides (often incorporating metal ions such as boron,

magnesium or aluminum) show similar properties to BaX_2, having a light yield between 10,000 and 40,000 photons/MeV and longer decay times, mostly above 500 ns and even above one microsecond (µs). Europium doped calcium halides (CaX_2) also present very high–light yields, in particular CaI_2, which shows a light yield above 100,000 photons/MeV, but have longer decay times than their barium counterparts. Cesium–barium, and cesium–calcium halide crystals also show remarkably high–light yields, as shown in Table 4, but their decay times is also significantly longer, often in the range of a few µs. Finally. we mention strontium halides, which are featured in Figure 4g–j, which also show a good light yield. In particular $SrI_2{:}Eu^{2+}$ yields 85,000 photons/MeV. The energy resolution of these Eu^{2+} doped scintillators is still excellent, usually between 3% and 4% at 662 keV. However, the few-hundred-ns lifetime of these scintillators are still much slower than the few-tens of ns lifetime of Ce^{3+} doped scintillators featured in the previous section.

Table 4. Overview of some Eu^{2+} and Yb^{2+} doped scintillators. The same convention as in Table 1 is used.

Scintillator	ρ (g/cm^3)	Z_{eff}	Light Yield (photons/MeV)	Energy Resolution (%, at 662 keV)	λ (nm)	τ (ns)	Ref.
$BaCl_2{:}Eu^{2+}$	3.89	49.8	19,400	8.8	402	390	[123]
$BaBr_2{:}Eu^{2+}$	4.78	47.8	15,700	11.0	404	585	[123]
$BaI_2{:}Eu^{2+}$	5.15	54.1	59,000	8.0	425	610	[124]
$BaFI{:}Eu^{2+}$	5.45	49.3	55,000	8.5	405	584	[125]
$BaClBr{:}Eu^{2+}$	4.50	44.2	52,000	3.6	407	484	[126]
$BaClI{:}Eu^{2+}$	4.60	49.4	54,000	9.0	410	-	[127]
$BaBrI{:}Eu^{2+}$	5.20	50.3	97,000	3.4	412	432	[128]
$Ba_2SiO_4{:}Eu^{2+}$	5.47	40.9	40,000	-	505	582	[129]
$BaKPO_4{:}Eu^{2+}$	4.14	34.6	35,000	-	425	540	[129]
$Ba_2Si_3O_8{:}Eu^{2+}$	3.97	35.1	35,000	-	505	1296	[129]
$BaSi_2O_5{:}Eu^{2+}$	3.73	33.4	30,000	-	520	2800	[129]
$Ba_3(PO_4)_2{:}Eu^{2+}$	5.25	38.8	27,000	-	420	459	[129]
$Ba_3P_4O_{13}{:}Eu^{2+}$	4.10	34.9	25,000	-	440	669	[129]
$Ba_5Si_8O_{21}{:}Eu^{2+}$	3.93	34.7	20,000	-	453	742	[129]
$BaNaPO_4{:}Eu^{2+}$	4.27	34.5	20,000	-	450	566	[129]
$Ba_3B(PO_4)_3{:}Eu^{2+}$	4.17	35.4	18,000	-	418	698	[129]
$Ba_2ZnSi_2O_7{:}Eu^{2+}$	4.75	36.2	16,000	-	505	748	[129]
$BaAl_{10}MgO_{17}{:}Eu^{2+}$	3.77	24.4	16,000	-	459	1100	[129]
$Ba_2B_5O_9Cl{:}Eu^{2+}$	3.75	32.8	11,000	-	420	640	[129]
$Ba_2MgSi_2O_7{:}Eu^{2+}$	4.26	35.8	10,000	-	505	692	[129]
$CaF_2{:}Eu^{2+}$	3.40	15.5	24,000	-	430	940	[130]
$CaBr_2{:}Eu^{2+}$	3.35	35.3	36,000	9.1	448	2500	[131]
$CaI_2{:}Eu^{2+}$	3.96	48.0	110,000	8.0	470	790	[132]
$Cs_2BaCl_4{:}Eu^{2+}$	3.75	44.9	30,000	-	431	-	[127]
$Cs_2BaBr_4{:}Eu^{2+}$	4.40	47.0	25,000	-	441	-	[127]
$Cs_2BaI_4{:}Eu^{2+}$	4.50	54.0	17,000	-	462	-	[127]
$CsBa_2Br_5{:}Eu^{2+}$	4.48	46.2	92,000	-	430	844	[133]
$CsBa_2I_5{:}Eu^{2+}$	4.90	54.0	102,000	2.6	435	1200	[128]
$CsBa_2I_5{:}Yb^{2+}$	4.90	54.0	54,000	5.7	414	870	[134]
$CsCaCl_3{:}Eu^{2+}$	3.00	44.3	18,000	8.9	445	5050	[135]
$CsCaBr_3{:}Eu^{2+}$	3.72	46.6	28,000	9.3	447	6097	[136]
$CsCaI_3{:}Eu^{2+}$	4.06	54.0	38,500	8.0	450	1720	[135]
$CsSrCl_3{:}Eu^{2+}$	2.57	38.9	33,400	11.5	442	2700	[137]
$CsSrBr_3{:}Eu^{2+}$	3.34	42.1	31,300	9.0	448	2500	[137]
$CsSrI_3{:}Eu^{2+}$	3.74	51.4	65,000	5.9	450	3300	[138]
$K_2BaI_4{:}Eu^{2+}$	4.12	49.4	63,000	2.9	448	1500	[139]
$KBa_2I_5{:}Eu^{2+}$	4.47	52.2	90,000	2.4	444	1700	[139]
$SrBr_2{:}Eu^{2+}$	4.22	36.1	20,000	7.0	410	-	[132]
$SrI_2{:}Eu^{2+}$	4.60	49.4	85,000	3.7	422	1200	[140]
$SrI_2{:}Yb^{2+}$	4.60	49.4	56,000	4.4	414	610	[134]
$SrClI{:}Eu^{2+}$	4.10	42.8	70,000	-	414	-	[127]
$SrBrI{:}Eu^{2+}$	4.90	44.2	47,000	-	418	-	[127]

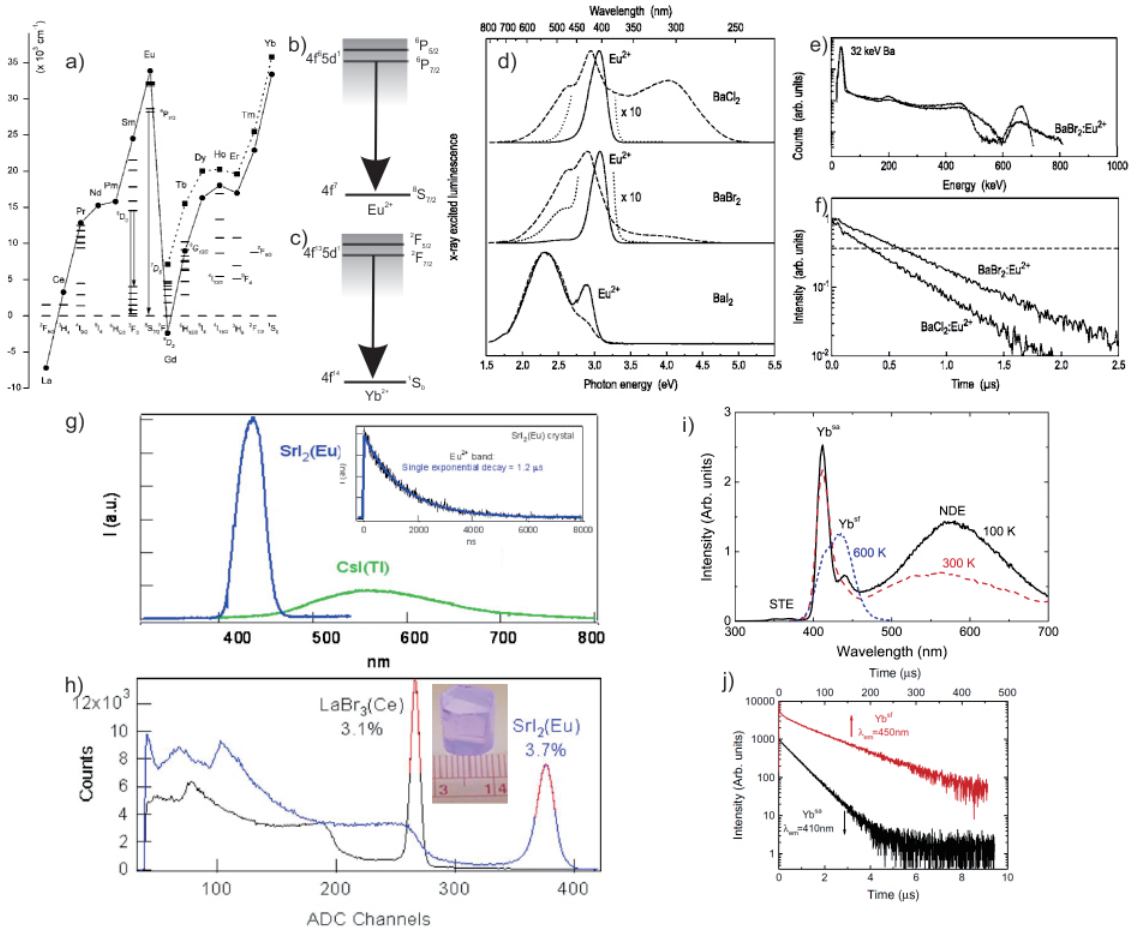


Figure 4. Divalent lanthanide-doped scintillators: (**a**) $4f^n$ energy level scheme of the free divalent lanthanides. The first fd level is connected with the full line. (**b**,**c**) Singlet 5d→4f allowed transition of Eu^{2+} and Yb^{2+}, respectively. (**d**) Normalized X-ray excited luminescence spectra of undoped (dashed curves) and Eu^{2+} doped (solid curves) BaX_2 ($X = Br, Cl, I$). Parts of the spectra of the Eu^{2+} doped samples (dotted curves) are blown up ten times as indicated. All spectra were recorded at RT. (**e**) Pulse height spectrum of a ^{137}Cs source measured with undoped and Eu^{2+} doped $BaBr_2$ crystals. (**f**) Scintillation decay curves for Eu^{2+} doped BaX_2 ($X = Br, Cl$) crystals. (**g**) Beta-excited emission spectrum from Eu^{2+} doped SrI_2 compared to that of $CsI{:}Tl$. The inset exhibits time-resolved emission decays acquired by excitation with 30 ns laser pulses at 266 nm. (**h**) Pulse-height spectra acquired of a $SrI_2{:}Eu^{2+}$ crystal yielding an energy resolution of 3.7% at 662 keV. In the inset, a photo from $SrI_2{:}Eu^{2+}$ crystal under 254 nm excitation. (**i**) X-ray excited emission spectra of SrI_2: 0.5% Yb^{2+} measured at 100, 295, and 600 K. The 410 nm and 450 nm bands are spin-allowed (Yb^{sa}) and spin-forbidden (Yb^{sf}) Yb^{2+} 5d→4f transitions, respectively. (**j**) Time-resolved emission at 295 K of black and red curves from SrI_2: 0.5% Yb^{2+} recorded under 340 nm excitation by monitoring the Yb^{sa} and Yb^{sf} emission, respectively. Figures reproduced from (**a**) Dorenbos, P., *J. Phys. Condens. Matter* **2003**, 15, 575–594. 2003 by IOP Publishing; (**d**–**f**) Selling, J. et al., *J. Appl. Phys.* **2007**, 101, 034901-1–034901-5. 2007 by AIP Publishing; (**g**,**h**) Cherepy, N. et al., *APL. Phys. Lett.* **2008**, 92, 083508-1–083508-3. 2008 by AIP Publishing; (**i**,**j**) Alekhin, M. S. et al., *Opt. Mater.* **2014**, 37, 382–386. 2014 by Elsevier.

5. Perovskite Scintillators: Advantages and Limitations

Solution-processable perovskites (SPPs), either organic-inorganic hybrid perovskites (HOIPs) or fully inorganic perovskites (FIPs), have gathered recent attention for their remarkable capabilities as light-harvesting materials in solar cells and high electroluminescence efficiency in light-emitting diodes. Unlike perovskites like $LuAlO_3$ and $YAlO_3$ we discussed in the previous section, this new class of perovskites can be processed from solution, not requiring high temperature or vacuum deposition

technologies, making these materials easier and cheaper to process. In addition, as the light yield of a scintillator is inversely proportional to the bandgap, SPPs, which often have a smaller bandgap than other scintillator materials, are expected to potentially reach extremely high–light yields, up to 250,000 photons/MeV [141]. We note that the estimated possible light yield is only based on the bandgap with an assumption that quantum (Q) and transfer efficiencies (S) are in unity, see Section 2.3 about the light yield. SPPs have been shown to exhibit a large absorption coefficient, in particular in bulk single crystals [142–144], to efficiently convert the X-ray photons into charge carriers [145–147] and have efficient electroluminescence quantum yield [148]. In particular, perovskite nanocrystals have shown remarkable electroluminescence, reaching record high efficiencies above 57 $cd\ A^{-1}$ [149]. Some early works on SPP scintillators started fifteen years ago [150] but until now, the research has very slow progress [21,151]. Recently tested SPPs have shown good light yields at low temperatures, their efficiency decreases with temperature and room-temperature light yields are much less than the expected theoretical value for HOIPs. Methylmmonium lead halide crystals (Figure 5a,b) have shown a light yield lower than 1000 photons/MeV at room temperature [22], while the 2D layered perovskites such as 2,2-(ethylenedioxy)bis(ethylammonium) lead chloride (Figure 5c) and 2-phenylethylammonium lead bromide have shown light yields of 9000–14,000 photons/MeV [22,152,153]. The visible and X-ray stimulated luminescence of these materials is shown in Figure 5d–g demonstrating a wide array of emission spectra for these materials. Although the light yield for SPPs has not been as high as expected, these material show very low afterglow (Figure 5h) and the decay time has been shown to be very short, ranging from few ns to tens of ns (Figure 5i–k), which makes HOIPs very suitable materials for fast and real-time applications. In addition, HOIPs have shown good energy discrimination, i.e., the capability to differentiate between different energies of incident radiation, particularly characterized by an incident energy-dependent emission spectrum of the scintillator as illustrated in Figure 5l,m. A main limitation of HOIPs is their relative low density and effective atomic number, due to the presence of organic cations containing mainly carbon, hydrogen and nitrogen, making the absorption length of HOIPs larger compared to inorganic scintillators. The presence of organic cations also makes these materials more susceptible to chemical degradation under irradiation, potentially lowering their radiation hardness.

Fully inorganic SPPs, such as single crystals of $CsPbBr_3$ (Figure 6), have been recently investigated for their scintillation properties [141]. Unlike HOIPs, these materials do not contain any organic molecules, but only inorganic ions; they still benefit for being soluble and thus, can also be processed by solution methods. It has been shown that these materials are generally more stable, both thermally and to environmental conditions, than their hybrid organic-inorganic counterparts [154]. In addition, the lack of any organic molecules within the SPP, which are liable to decomposition under UV and X-ray exposure, is expected to increase radiation hardness as well. As shown in Figure 6a and b, X-ray Photoelectron Spectroscopy (XPS) has been used to detect the composition of the SPP scintillators, including the impurities which may be present on the sample. Comparing $MAPbBr_3$ and $CsPbBr_3$ in regard of their carbon and nitrogen content we see that $MAPbBr_3$ has significant presence of both elements, deriving from presence of the methylammonium ion. On the other hand $CsPbBr_3$ shows no nitrogen at all, as expected from the ideal material composition. However, $CsPbBr_3$ still shows presence of carbon, which is probably caused by organic solvent molecules trapped within the material. Our co-workers Xie et al. have presented low to high temperature mapping of X-ray excited luminescence from $CsPbBr_3$ (Figure 6c,d). From the figure, we observe that the X-ray excited luminescence is very high at low temperature, but significantly decreases at higher temperatures. At room temperature, the light yield is less than 1000 photons/MeV [141] similar with methylammonium lead halide crystals [22] and therefore of no real practical interests as scintillators.

Overall solution-processable perovskites are a very promising class of materials for scintillation applications, and although research on these materials is still in its infancy they have shown already remarkable properties.

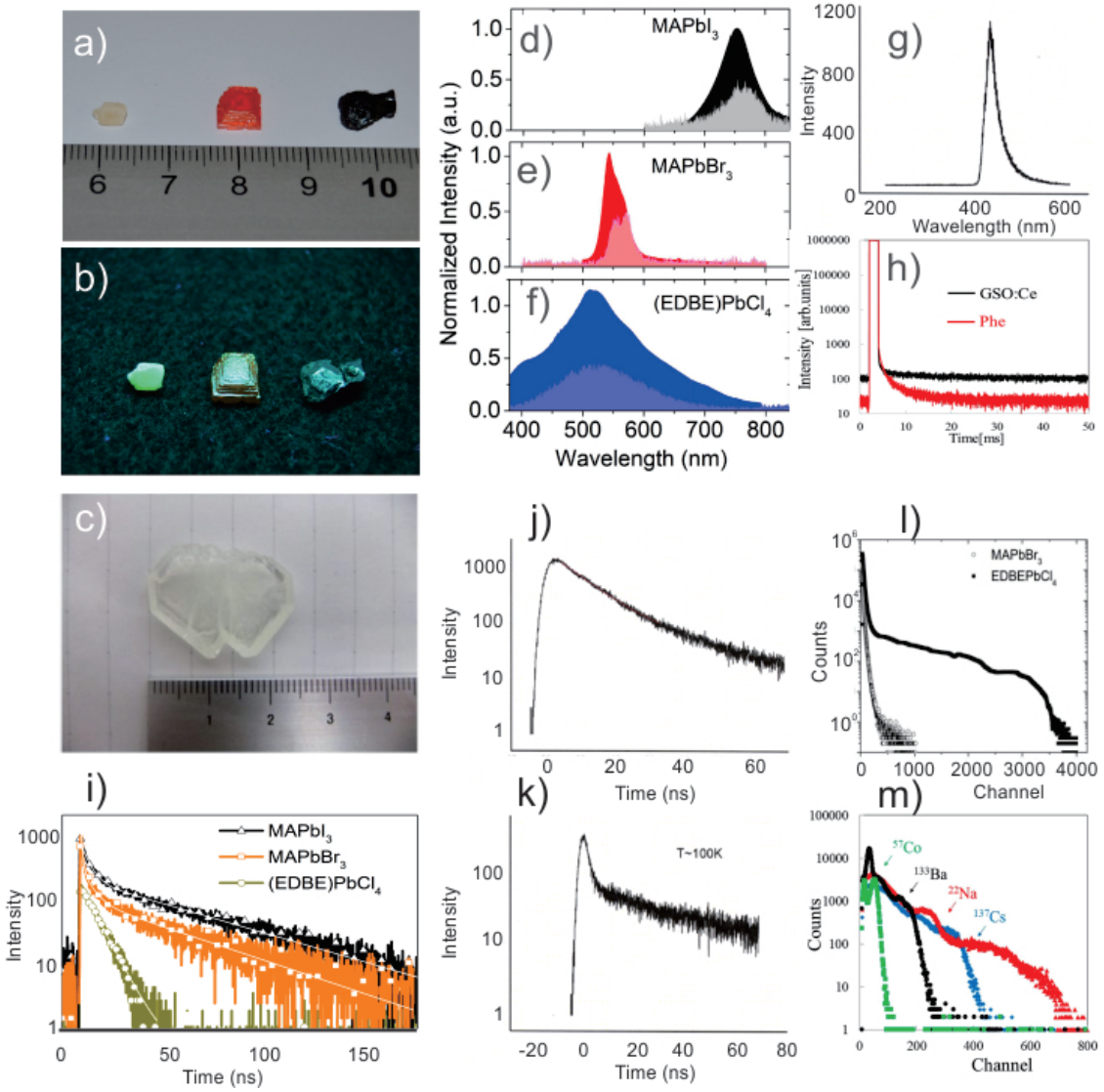


Figure 5. Perovskite single crystal scintillators: (**a**) A photographs of the large single crystals of hybrid lead halide perovskites. From left to right: $(EDBE)PbCl_4$ (two-dimensional scintillator), $MAPbBr_3$ and $MAPbI_3$ (both are three-dimensional scintillators). (**b**) Glow of the crystals under ultraviolet lamp excitation from the above crystals. (**c**) Another photograph of large two-dimensional perovskite ($(C_6H_5C_2H_4NH_3)_2PbBr_4$) or *Phe*). (**d**,**e**,**f**) X-ray excited luminescence (light color area) and photoluminescence (dark color area) spectra of three crystals in (**a**) with excitation wavelengths for photoluminescence of 425, 500, and 330 nm, respectively. Photoluminescence and X-ray excited luminescence spectra were normalized to their maxima, and normalized X-ray excited luminescence spectra were divided by a factor of two for clarity. (**g**) X-ray excited emission spectra of Phe. (**h**) X-ray induced afterglow time profiles of *Phe* with that of $Gd_2SiO_3:Ce^{3+}$ as a comparison. (**i**) Time-resolved emission curves of $(EDBE)PbCl_4$, $MAPbBr_3$ and $MAPbI_3$ recorded under 330, 370 and 640 nm excitation and by monitoring 520, 540 and 766 nm emission, respectively. (**j**,**k**) Scintillation decay curves of Phe under pulsed X-ray excitation. (**l**) Pulse height spectra of $(EDBE)PbCl_4$ and $MAPbBr_3$ under ^{137}Cs γ-ray excitation. (**m**) Pulse height spectra of *Phe* under different γ-ray excitations. All measurements beside that in (**k**) (100 K) were measured at RT. Figures reproduced from (**a**,**b**,**d**,**e**,**f**,**i**,**l**) Birowosuto, M. D., *Sci. Rep.* **2016**, 6, 37254. 2016 by Springer Nature; (**c**,**h**,**m**) Kawano, N. et al., *Sci. Rep.* **2017**, 7, 14754. 2017 by Springer Nature; (**g**,**j**,**k**) van Eijk, C. W. E. et al., *IEEE Nucl. Sci. Symp. Conf. Rec.* **2008**, N69-3, 3525-3538. 2008 by IEEE.

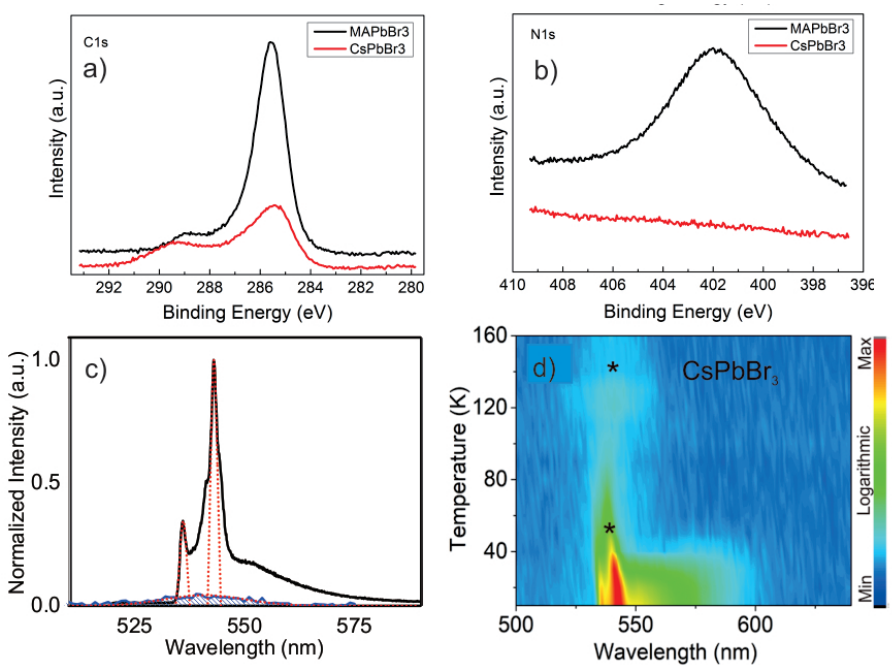


Figure 6. All inorganic scintillator, $CsPbBr_3$. (**a**,**b**) X-ray photoemission spectra of the C1s and N1s core levels of $MAPbBr_3$ and $CsPbBr_3$ crystals. (**c**) Low- (10 K) and high-temperature (150 K) X-ray-excited luminescence spectra shown by white and blue-shaded area, respectively. (**d**) Temperature mapping of XL spectra from 10 to 160 K. Figures reproduced from (**c**,**d**) Aozhen, X. et al., *J. Phys. Chem. C* **2018**, 122, 16265–16273. 2018 by ACS.

6. Nanotechnology Improvements for Scintillators

Nanostructured scintillators have been a natural progression of scintillators following the advancement of nanotechnology techniques for the light sources [155]. Both nanostructuring of scintillators and quantum dot (QD) or nanocrystal scintillators have been shown to have improved performance over unpatterned scintillators. Nanostructuring of scintillators is mostly in the form of photonic crystal (PhC). For inorganic scintillators, the density required to to show an efficient absorption probability renders it inefficient for scintillation light to be collected by the photodetector. High refractive index of the scintillator causes the light to undergo total internal reflection, thus, resulting in absorption loss and delay of output light to the photodetector. Photonic crystal has been used to controllably improve index matching between the scintillator and photodetector, thus, improving the light extraction efficiency. The concepts and modeling of the enhanced extraction mechanism have been detailed in a review by Knapitsch and Lecoq in 2014 [156]. Further extensive reviews on the works on photonic crystal on scintillators have been done in 2018 by Salomoni et al. [157]. In this review we discuss systemically the nanostructuring methods, as well as QD and nanocrystal scintillators as another alternative to improve scintillating performance. Also, the current trend of nanotechnology in perovskite will be the focus of our discussion.

6.1. Nanostructuring of Bulk Scintillators

There are several methods to create nanostructures in bulk scintillators. Figure 7a shows an example of photonic crystals that have been attached on top of a scintillator crystal. In this section, we first discuss bottom-up process that can be performed by creating self-assembled colloidal patterns on top of scintillators. Secondly, we discuss top-down process for creating nanostructures of masking materials on the top of bulk scintillator crystals or nanostructures on the scintillator material itself, with the focus on nanostructuring methods in the new solution-based perovskite materials.

6.1.1. Self-Assembled Methods

Figure 7b, c, and d shows the schematic and SEM images of photonic crystal structure covering the surface of $Lu_xY_{2-x}SiO_5$ scintillator. The PhC structure was realized by ALD deposition of TiO_2 on hexagonally close packed self-assembled polystyrene nanospheres. Higher light extraction efficiency was demonstrated which led to higher coincidence timing resolution, which may improve timing characteristic for time-of-flight detection system [158].

6.1.2. Lithographic Methods

- Electron beam lithography
  Electron beam lithography (EBL) is used to create patterns on a resist layer. Such method gives highly accurate pattern but due to its serial nature of the pattern writing, it is rather impracticable for mass production. The patterns are then transferred by etching techniques such as Reactive Ion Etching (RIE) to an intermediate layer such as silicon nitride (Si_3N_4), if the scintillator material is not etchable by standard lithographic methods. Figure 7a shows photonic crystals of Si_3N_4 patterned by EBL on top of Lu_2SiO_5 scintillator [156]. Light yield improvement of 20-60% compared to unpatterned scintillator is demonstrated [159]. Recently our co-workers Hou et al. demonstrated high enhancement of PL intensity from photonic crystal of perovskite thin film. The PMMA patterns are transferred directly to the perovskite material, without any intermediate layer, to form the perovskite photonic crystal [160]. This ability to pattern hygroscopic perovskite material, combined with excellent scintillation properties of perovskite material will be promising for future applications. Figure 7e,f shows the refractive index of $MAPbI_3$ and the SEM picture of perovskite photonic crystals, respectively.
- Soft X-ray interference lithography
  Using a mask consisting of four diffraction gratings creating interference patterns, conical holes of 45 nm thick of PMMA is patterned on BGO. TiO_2 layer is then deposited using Atomic Layer Deposition (ALD). The high refractive index of the conformal TiO_2 layer enables light extraction enhancement of up to 95.1% [161]. This technique is mass scalable however the patterns are limited to those which can be produced from wave interference.
- Direct thermal nanoimprint lithography
  Using commercially available nanoimprinting stamp [162], low lasing threshold of 3.8 μ J/cm^2 has been demonstrated from 2D photonic crystal on $MAPbI_3$. This low threshold shows the good quality of the nanostructured perovskite which might be potential for scintillating applications. The nanoimprinting technique also gives the advantage of mass scalability.

6.1.3. Focused Ion Beam (FIB) Milling

Nanostructuring perovskite film in the form of FIB milled nanogratings and nanoslits has been demonstrated by Gholipour et al. as shown in Figure 7g,h [163]. Nanostructuring the perovskite thin film in subwavelength periodic grating is shown to enhance the photoluminescence intensity by three folds and the emission rate by four folds. We expect that such enhancement may improve scintillation light collection.

6.2. QD and Nanocrystal Scintillators

Scintillating material in the form of nanocrystals has the advantage of avoiding defects which may be imparted during pattern transfer processes in the nanostructuring methods. Earlier reports on nanocrystal scintillators focused on II-VI QDs whereas perovskite nanocrystals are currently emerging is a promising scintillating material. Nevertheless, the question of the energy deposition in the nanocrystal during a energy relaxation mechanism, which shows most of their mean free path larger than the particle size, is still under study [164].

6.2.1. II-VI QDs

II-VI QDs have been investigated as scintillation material which theoretically holds advantage over its bulk counterparts due to its quantum confinement effects. Experimentally, X-ray excited luminescence of $CdTe$ QDs has been investigated and resolution of 5 lines/mm has been demonstrated [165]. In addition, the $CdTe$ QDs have fast decay, no afterglow, high stopping power, and superior spectral match to the charge-coupled device (CCD) detector [166]. Cadmium-free QDs are now trending in scintillator research and they are easy to implement with many kinds of photodetectors. They are also more environmentally friendly than cadmium QDs [167]. Zinc sulfide QDs doped with magnesium sulfide, $ZnS(MgS)$, show good proportionality and high sensitivity [168]. However, the absorption length of these QDs at 100 keV is eight times longer than that of $CdTe$ QDs. The low absorption is due to the low mass density and effective atomic number of $ZnS(MgS)$ [168]. Furthermore, as an advantage above bulk scintillators, QDs can be embedded inside microstructured fiber, which may be potential for scope-platform imaging applications.

6.2.2. Perovskite Nanocrystals

A new class of nanostructures in the form of perovskite nanocrystals has emerged to be a promising scintillation material. In perovskite $CsPbBr_3$, we can improve the light yield through quantum confinement as the quantum efficiency was reported to be more than 80 % [169]. $CsPbBr_3$ nanocrystals have been demonstrated (by Chen et al. [170]) to have a light yield of 33,000 photons/MeV (54% light yield of CsI:Tl). This is much higher yield than that of $CsPbBr_3$ single crystals with less than 1000 photons/MeV [141]. Additionally, X-ray excited emission wavelength of $CsPbX_3(X = Cl, Br, I)$ nanocrystals can be easily tuned depending on the anionic component of the perovskite, as shown in Figure 7i. This tunability is also an advantage above a conventional bulk scintillator. Figure 7j shows multicolour X-ray excited luminescence image from three different anionic components of $CsPbX_3$ (orange: $CsPbBr_2I$; green: $CsPbBr_3$; blue: $CsPbClBr_2$) as captured by standard photographic camera. The lowest detectable dose rate for X-ray detection is surprisingly low (13 nanograys per second). The response time to X-ray is fast and does not have afterglow effect, which offers promise for dynamic real-time X-ray imaging. Furthermore, nanocrystal perovskite is solution processable at low temperature and practically scalable for mass scale production. Since the use of perovskite nanocrystals as scintillators is still very recent, the investigation for the novel lead-free perovskite nanocrystals, such as bismuth-based materials, is tantalizing.

A recently developed proof-of-concept prototype of nanocrystal perovskite scintillator is shown schematically in Figure 7k. It consists of a protective aluminum foil cover, 75 µm nanocrystal perovskite layer, α-Si photodiode arrays and TFT sensor panel. The nanocrystal perovskite scintillator shows a modulation transfer function of 0.72 at a spatial resolution of 2.0 line pairs per millimetre, which implies much higher spatial resolution than that of commercially used CsI:Tl-based flat-panel X-ray detectors. The packaged prototype is shown in Figure 7l. The perovskite scintillator prototype is then used to image the internal circuitry of an iPhone as shown in Figure 7m. Separately, Heo et al. demonstrated that, compared to a commercial $GOS:Tb$ detector, $CsPbBr_3$ nanocrystal scintillator exhibits higher ratio of light output power/absorptivity, faster response time, and higher spatial resolution [171]. All those results [170,171] are very promising for (nanocrystal) perovskite scintillators, showing that they have the potential to replace current scintillators as a low-cost, high yield alternative. However, it remains a challenge to ensure if such design can fully prevent signal crosstalks, which currently was prevented by designing multicolumn scintillators flat panel detectors.

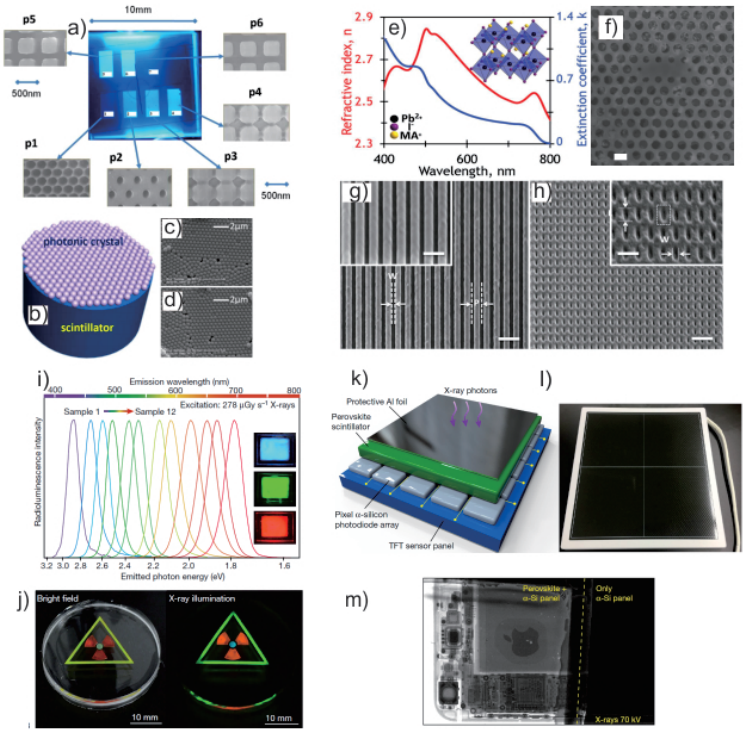


Figure 7. Nanotechnology improvements of scintillators. (**a**) Photonic crystals for the extraction efficiency improvements produced with e-beam lithography in Si_3N_4 on a scintillator. (**b**) Schematic illustration of the self-assembled photonic crystal structures covered on the surface of scintillator. (**c**,**d**) Scanning electron microscope image of self-assembled photonic crystals from polystyrene spheres. (**e**) Refractive index and extinction coefficient of $MAPbI_3$ obtained from ellipsometry while the inset shows the crystal structure. (**f**) Perovskite photonic crystals fabricated through electron-beam lithography. (**g**,**h**) Scanning electron microscope images of nanograting and nanoslit metamaterials from perovskite. (**i**) $CsPbX_3$ ($X = Cl, Br, I$) nanocrystals with tunable emission wavelength and high quantum efficiency. (**j**) Multicolour X-ray scintillation (left, bright-field imaging; right, X-ray illumination at a voltage of 50 kV) from perovskite nanocrystal scintillator. (**k**) Design for X-ray panels with perovskite nanocrystal film (75 μm thick). (**l**) Photograph of the packaged flat-panel detector. (**m**) X-ray images of an Apple iPhone acquired with the perovskite scintillator. Figures reproduced from (**a**) Salomoni, M. et al., *Crystals* **2018**, 8, 1–35. 2018 by MDPI; (**b**–**d**) Liu, J. et al., *Opt. Lett.* **2017**, 42, 987–990. 2017 by OSA. (**e**,**g**,**h**) Gholipour, B. et al., Advanced Materials. 2017, 29, 1604268. 2017 by Wiley. (**i**,**j**,**k**,**l**,**m**) Chen, Q. et al., Nature 2018, 561, 88–93. 2018 by Springer Nature.

7. Summary

We have shown the progress in the research of scintillators from the seventy-year-old earliest traditional scintillators, $NaI{:}Tl^+$ and $CsI{:}Tl^+$ [56], the first lanthanide-doped scintillators discovered in the late eighties, Ce^{3+}, Pr^{3+}, and Nd^{3+} doped LaF_3 [93] and YAG [118], to the very recent perovskite scintillators [22,170,171]. Lanthanide-doped scintillators already offer excellent scintillation properties. $CaI_2{:}Eu^{2+}$ [132] and $LuI_3{:}Ce^{3+}$ [89] have more than 100,000 photons/MeV light yield while $LaBr_3{:}Ce^{3+}$ with Sr^{2+} and Ca^{2+} co-doping has the best energy resolution of 2.0 % [86]. Finally, $LaF_3{:}Nd^{3+}$ [93] and $PrBr_3{:}Ce^{3+}$ [96] have the fastest scintillation lifetime of 6 ns. Various trends in fundamental limit in light yields and lifetimes, scintillation mechanisms, and the relationship between Stokes shifts, self absorptions, and decay time lengthening were discussed previously for lanthanide scintillators [83]. From the same review, we notice that there are not many rooms for scintillation properties' improvements [83]. However, the price for the scintillators still remains the largest component in the X- and γ-ray detectors. It is still costly because the crystals are grown through complicated procedures inside high temperature oven furnace. Regarding lanthanide scintillators,

extraction and reuse of these lanthanide ions is complicated while the supply is restricted. Therefore, some researchers are looking at other potential materials for scintillators, such as perovskite halide single crystals [150]. These crystals can be fabricated through a low-cost solution process at low temperatures of $<$100 °C. They also have small bandgaps, large effective atomic number, and high mass density to provide high–light yield conversions and efficient X- and γ-ray absorptions, respectively. Finally, the exciton lifetimes of perovskite halide materials are in few ns, which are comparable with Ce^{3+} doped scintillators [83]. However, there were not much progress for the perovskite scintillators [21,151] while the materials are still the same since fifteen years ago, e.g., phenethylamine halides [153]. Until recently, we introduced other halide-perovskite single-crystal scintillators as potential scintillators [22,141]. However, the light yields of halide perovskite scintillators are still lower than those in the best-recorded scintillators and, therefore, looking at two-dimensional perovskite materials [22], nanostructure fabrications [156], and nanocrystal synthesis [170] may hold the keys for better perovskite scintillators. In general, such studies on those novel materials pave the way towards low-cost and excellent scintillators for medical and security applications.

Author Contributions: F.M., L.T., and M.D.B. prepared and wrote the concept of the review. A.X. prepared the perovskite samples. A performed the XPS measurements for perovskite samples. W.D. performed the X- and γ-ray measurements for perovskite samples. C.D. and W.D. contributed to the critical points from the expertise. S.Z., H.W., P.C., W.D., C.D., C.Dang, and M.D.B. contributed to the reading and writing of the manuscript.

Acknowledgments: F.M., M.D.B. and C.Dang acknowledge support from Thales, France. L.T., M.D.B. and H.W. acknowledge support from Ministry of Education, Singapore under grant No. MOE2016-T2-1-052. H.W. also acknowledges support from National Research Foundation, Singapore under grant No. NRF-CRP12-2013-04. S.Z. acknowledges support from European Union's Horizon 2020 research and innovation programme under the Marie Sklodowska-Curie grant agreement No. 798916. C.D. acknowledges support from Ministry of Education, Singapore under grant No. Tier-1 RG 178/17.

Conflicts of Interest: The authors declare no conflict of interest.

References

1. Rodnyi, P.A. *Physical Processes in Inorganic Scintillators*, 1st ed.; CRC Press: Boca Raton, FL, USA, 1997.
2. Knoll, G. *Radiation Detection and Measurement*; Wiley: Hoboken, NJ, USA, 2000.
3. Lecoq, P.; Gektin, A.; Korzhik, M. *Inorganic Scintillators for Detector Systems*, 2nd ed.; Springer International Publishing: Berlin, Germany, 2017.
4. Russo, P. *Handbook of X-ray Imaging: Physics and Technology*; CRC Press: Boca Raton, FL, USA, 2018.
5. Lille, S.; Marshall, W. *Mammographic Imaging*; Wolters Kluwer: South Holland, The Netherlands, 2018.
6. Attix, F. *Introduction to Radiological Physics and Radiation Dosimetry*; Wiley: Hoboken, NJ, USA, 2004.
7. Webb, W.R.; Major, N.M. *Fundamentals of Body CT*; Elsevier Health Sciences: Amsterdam, The Netherlands, 2014.
8. Nikl, M. Scintillation detectors for X-rays. *Meas. Sci. Technol.* **2006**, *17*, R37. [CrossRef]
9. Bailey, D.L.; Townsend, D.W.; Valk, P.; Maisey, M. *Positron Emission Tomography*; Springer: London, UK, 2005.
10. Barkhausen, J.; Rody, A.; Schäfer, F.K.W. *Digital Breast Tomosynthesis: Technique and Cases*; George Thieme Verlag KG: Stuttgart, Germany, 2016.
11. Grajo, J.R.; Patino, M.; Prochowski, A.; Sahani, D. Dual energy CT in practice: Basic principles and applications. *Appl. Rad.* **2016**, *45*, 6–12.
12. Anger, H.O. Scintillation Camera. *Rev. Sci. Instrum.* **1958**, *29*, 27–33. [CrossRef]
13. MacAllister, D.; Miller, K.; Yang, C.; Graham, S. Application of X-ray CT scanning to determine gas/water relative permeabilities. *SPE Form. Eval.* **1993**, *3*, 184–188. [CrossRef]
14. Dujardin, C.; Auffray, E.; Bourret-Courchesne, E.; Dorenbos, P.; Lecoq, P.; Nikl, M.; Vasilév, A.N.; Yoshikawa, A.; Zhu, R. Needs, Trends, and Advances in Inorganic Scintillators. *IEEE Trans. Nucl. Sci.* **2018**, *65*, 1977–1997. [CrossRef]
15. Nikl, M.; Yoshikawa, A. Recent R&D Trends in Inorganic Single-Crystal Scintillator Materials for Radiation Detection. *Adv. Opt. Mater.* **2015**, *3*, 463–481.
16. Blasse, G. Scintillator Materials. *Chem. Mater.* **1994**, *6*, 1465–1467. [CrossRef]
17. Röntgen, W.C. On a New Kind of Rays. *Science* **1896**, *3*, 227–231. [CrossRef]
18. Weber, M.J. Inorganic scintillators: Today and tomorrow. *J. Lumin.* **2002**, *100*, 35–45. [CrossRef]

19. Brooks, F. Development of organic scintillators. *Nucl. Instrum. Methods Phys. Res.* **1979**, *162*, 477–505. [CrossRef]
20. Lecoq, P. Development of new scintillators for medical applications. *Nucl. Instrum. Methods Phys. Res.* **2016**, *809*, 130–139. [CrossRef]
21. van Eijk, C.W.E.; de Haas, J.T.M.; Rodnyi, P.A.; Khodyuk, I.V.; Shibuya, K.; Nishikido, F.; Koshimizu, M. Scintillation properties of a crystal of $(C_6H_5(CH_2)_2NH_3)_2PbBr_4$. In Proceedings of the 2008 IEEE Nuclear Science Symposium Conference Record, Dresden, Germany, 19–25 October 2008; pp. 3525–3528.
22. Birowosuto, M.D.; Cortecchia, D.; Drozdowski, W.; Brylew, K.; Lachmanski, W.; Bruno, A.; Soci, C. X-ray Scintillation in Lead Halide Perovskite Crystals. *Sci. Rep.* **2016**, *6*, 37254. [CrossRef] [PubMed]
23. Nabet, B. *Photodetectors, Materials, Devices and Applications*; Woodhead Publishing: Sawston, UK, 2016.
24. van Eijk, C.W.E. Fast scintillators and their applications. *Radiat. Meas.* **1993**, *21*, 5–10. [CrossRef]
25. van Eijk, C.W.E.; Dorenbos, P.; Visser, R. Nd^{3+} and Pr^{3+} doped inorganic scintillators. *IEEE Trans. Nucl. Sci.* **1994**, *41*, 738–741. [CrossRef]
26. Lempicki, A.; Wojtowicz, A.; Berman, E. Fundamental limits of scintillator performance. *Nucl. Instrum. Methods Phys. Res. A* **1993**, *333*, 304–311. [CrossRef]
27. Rodnyi, P.A.; Dorenbos, P.; van Eijk, C.W.E. Energy Loss in Inorganic Scintillators. *Phys. Stat. Sol. B* **1995**, *187*, 15–29. [CrossRef]
28. Dorenbos, P. Scintillation mechanisms in Ce^{3+} doped halide scintillators. *Phys. Stat. Sol. A* **2005**, *202*, 195–200. [CrossRef]
29. Hall, H. The Theory of Photoelectric Absorption for X-rays and y-Rays. *Rev. Mod. Phys.* **1936**, *29*, 358–397. [CrossRef]
30. Eisenberg, P.; Platzman, P. Compton Scattering of X Rays from Bound Electrons. *Phys. Rev. A* **1970**, *2*, 415–423. [CrossRef]
31. Hubbell, J. Electron–positron pair production by photons: A historical overview. *Rad. Phys. Chem.* **2006**, *75*, 614–623. [CrossRef]
32. Kinchin, G.H.; Pease, R.S. The Displacement of Atoms in Solids by Radiation. *Rep. Prog. Phys.* **1955**, *18*, 1. [CrossRef]
33. Frenkel, J. Über die Wärmebewegung in festen und flüssigen Körpern. *Z. Phys.* **1926**, *35*, 652–669. [CrossRef]
34. Karim, D.P.; Aldred, A.T. Localized level hopping transport in $La(Sr)CrO_3$. *Phys. Rev. B* **1979**, *20*, 2255–2263. [CrossRef]
35. Shepherd, J.A.; Gruner, S.M.; Tate, M.W.; Tecotzky, M. Study of afterglow in X-ray phosphors for use on fast-framing charge-coupled device detectors. *Opt. Eng.* **1997**, *36*, 36–36–11. [CrossRef]
36. Blasse, G. New Luminescent Materials. *Chem. Mater.* **1989**, *3*, 294–301. [CrossRef]
37. Kerisit, S.; Rosso, K.M.; Cannon, B.D.; Gao, F.; Xie, Y. Computer simulation of the light yield nonlinearity of inorganic scintillators. *J. Appl. Phys.* **2009**, *105*, 114915. [CrossRef]
38. Dujardin, C.; Pedrini, C.; Blanc, W.; Gacon, J.C.; van't Spijker, J.C.; Frijns, O.W.V.; van Eijk, C.W.E.; Dorenbos, P.; Chen, R.; Fremout, A.; et al. Optical and scintillation properties of large crystals. *J. Phys. Condens. Matter* **1998**, *10*, 3061–3073. [CrossRef]
39. Wojtowicz, A.; Drozdowski, W.; Ptaszyk, M.; Galazka, Z.; Lefaucheur, J.L. Scintillation Light Yield of Ce-Doped LuAP and LuYAP Pixel Crystals. In Proceedings of the 8th International Conference on Inorganic Scintillators and Their Use in Scientific and Industrial Applications, Kharkov, Ukraine, 19–23 September 2005; Gektin, A.V., Ed.; National Academy of Sciences of Ukraine: Kiev, Ukraine, 2006; pp. 473–476.
40. N. ter Weele, D.; Schaart, D.; Dorenbos, P. The Effect of Self-Absorption on the Scintillation Properties of Ce^{3+} Activated $LaBr_3$ and $CeBr_3$. *IEEE Trans. Nucl. Sci.* **2014**, *61*, 683–688. [CrossRef]
41. Melcher, C.L. Scintillation Crystals for PET. *J. Nucl. Med.* **2000**, *41*, 1501–1505.
42. Melcher, C.L.; Schweitzer, S. Cerium-doped lutetium oxyorthosilicate: A fast, efficient new scintillator. *IEEE Trans. Nucl. Sci.* **1992**, *39*, 502–505. [CrossRef]
43. Tian, Y.; Cao, W.H.; Luo, X.X.; Fu, Y. Preparation and luminescence property of Gd_2O_2S:Tb X-ray nano-phosphors using the complex precipitation method. *J. Alloy. Compd.* **2007**, *433*, 313–317. [CrossRef]
44. Leblans, P.; Struye, L.; Willems, P. A new needle-crystalline computed radiography detector. *J. Digit. Imaging* **2000**, *13*, 117–120. [CrossRef] [PubMed]
45. Neitzel, U. Status and prospects of digital detector technology for CR and DR. *Radiat. Prot. Dosim.* **2005**, *114*, 32–38. [CrossRef]
46. Sawant, A.; Antonuk, L.E.; El-Mohri, Y.; Zhao, Q.; Li, Y.; Su, Z.; Wang, Y.; Yamamoto, J.; Du, H.; Cunningham, I.; et al. Segmented crystalline scintillators: An initial investigation of high quantum efficiency detectors for megavoltage X-ray imaging. *Med. Phys.* **2005**, *32*, 3067–3083. [CrossRef] [PubMed]

47. Schaefer-Prokop, C.; Neitzel, U.; Venema, H.W.; Uffmann, M.; Prokop, M. Digital chest radiography: an update on modern technology, dose containment and control of image quality. *Eur. Radiol.* **2008**, *18*, 1818–1830. [CrossRef]
48. Pititeeraphab, Y.; Laksanapanai, B.; Lertprasert, P.; Pintaviroo, C. X-ray-Detector with CMOS Sensor Camera. In Proceedings of the World Congress of Medical Physics and Biomedical Engineering, Seoul, Korea, 27 August–1 Septmber 2006; Magjarevic, R., Nagel, J.H., Eds.; Springer: Berlin/Heidelberg, Germany, 2006; pp. 813–816.
49. Rocha, J.; Minas, G.; Lanceros-Mendez, S. Optical coupling between scintillators and standard CMOS detectors. *Nucl. Instrum. Methods Phys. Res. A* **2006**, *556*, 281 –286. [CrossRef]
50. Takahashi, T.; Gunji, S.; Hirayama, M.; Kamae, T.; Miyazaki, S.; Sekimoto, Y.; Tamura, T.; Tanaka, M.; Yamasaki, N.Y.; Yamagami, T.; et al. Newly developed low background hard X-ray/gamma-ray telescope with the well-type phoswich counters. *IEEE Trans. Nucl. Sci.* **1993**, *40*, 890–898. [CrossRef]
51. Biswas, S.; Das, S.; Ghosh, S.; Nag, D.; Raha, S. Development of scintillator detector for detection of cosmic ray shower. *J. Instrum.* **2017**, *12*, C06026. [CrossRef]
52. Atac, M.; Streets, J.; Wilcer, N. Detection of cosmic ray tracks using scintillating fibers and position sensitive multi-anode photomultipliers. *AIP Conf. Proc.* **1998**, *422*, 251–256.
53. Bross, A.D. Applications for Large Solid Scintillator Detectors in Neutrino and Particle Astrophysics. *Nucl. Phys. B Proc. Suppl.* **2000**, *229–232*, 363–367. [CrossRef]
54. N. Annenkov, A.; Buzanov, O.; Danevich, F.; Georgadze, A.; Kim, S.; J. Kim, H.; D Kim, Y.; Kobychev, V.; Kornoukhov, V.; Korzhik, M.; et al. Development of CaMoO4 crystal scintillators for double beta decay experiment with 100-Mo. *Nucl. Instrum. Methods Phys. Res. A* **2008**, *584*, 334–345. [CrossRef]
55. Crookes, W. Certain Properties of the Emanations of Radium. *Chem. News* **1903**, *87*, 241.
56. Hofstadter, R. Alkali Halide Scintillation Counters. *Phys. Rev.* **1948**, *74*, 100–101. [CrossRef]
57. Porter, F.; Freedman, M.; Wagner, F.; Sherman, I. Response of NaI, anthracene and plastic scintillators to electrons and the problems of detecting low energy electrons with scintillation counters. *Nucl. Instrum. Methods Phys. Res.* **1966**, *39*, 35–44. [CrossRef]
58. Blahuta, S.; Bessiere, A.; Viana, B.; Dorenbos, P.; Ouspenski, V. Evidence and Consequences of Ce^{4+} in LYSO: Ce, Ca and LYSO: Ce, Mg Single Crystals for Medical Imaging Applications. *IEEE Trans. Nucl. Sci.* **2013**, *60*, 3134–3141. [CrossRef]
59. Nikl, M.; Kamada, K.; Babin, V.; Pejchal, J.; Pilarova, K.; Mihokova, E.; Beitlerova, A.; Bartosiewicz, K.; Kurosawa, S.; Yoshikawa, A. Defect Engineering in Ce-Doped Aluminum Garnet Single Crystal Scintillators. *Cryst. Growth Des.* **2014**, *14*, 4827–4833. [CrossRef]
60. Moretti, F.; Hovhannesyan, K.; Derdzyan, M.; Bizarri, G.A.; Bourret, E.D.; Petrosyan, A.G.; Dujardin, C. Consequences of Ca Codoping in YAlO3:Ce Single Crystals. *Chem. Phys. Chem.* **2017**, *18*, 493–499. [CrossRef]
61. Moszynski, M.; Balcerzyk, M.; Czarnacki, W.; Nassalski, A.; Szczęśniak, T.; Kraus, H.; Mikhailik, V.; Solskii, I. Characterization of $CaWO_4$ Scintillator at Room and Liquid Nitrogen Temperatures. *Nucl. Instrum. Methods Phys. Res. A* **2005**, *553*, 578–591. [CrossRef]
62. Bauer, R.; Weingart, R. Fabrication of thin NaI(TI) scintillation layers for low energy X-ray detection. *Nucl. Instrum. Methods Phys. Res.* **1967**, *55*, 55–60. [CrossRef]
63. Nagarkar, V.V.; Gupta, T.K.; Miller, S.R.; Klugerman, Y.; Squillante, M.R.; Entine, G. Structured CsI(Tl) scintillators for X-ray imaging applications. *IEEE Trans. Nucl. Sci.* **1998**, *45*, 492–496. [CrossRef]
64. van Eijk, C.; Dorenbos, P.; van Loef, E.; Krämer, K.; Güdel, H. Energy resolution of some new inorganic-scintillator gamma-ray detectors. *Rad. Meas.* **2001**, *33*, 521–525. [CrossRef]
65. Sakai, E. Recent Measurements on Scintillator-Photodetector Systems. *IEEE Trans. Nucl. Sci.* **1987**, *34*, 418–422. [CrossRef]
66. Moszyński, M.; Allemand, R.; Laval, M.; Odru, R.; Vacher, J. Recent progress in fast timing with CsF scintillators in application to time-of-flight positron tomography in medicine. *Nucl. Instrum. Methods Phys. Res.* **1983**, *205*, 239–249. [CrossRef]
67. Laval, M.; Moszyński, M.; Allemand, R.; Cormoreche, E.; Guinet, P.; Odru, R.; Vacher, J. Barium fluoride—Inorganic scintillator for subnanosecond timing. *Nucl. Instrum. Methods Phys. Res.* **1983**, *206*, 169–176. [CrossRef]
68. Derenzo, S.E.; Moses, W.W.; Cahoon, J.L.; Perera, R.C.C.; Litton, J.E. Prospects for new inorganic scintillators. *IEEE Trans. Nucl. Sci.* **1990**, *37*, 203–208. [CrossRef]

69. Kinloch, D.R.; Novak, W.; Raby, P.; Toepke, I. New developments in cadmium tungstate. *IEEE Trans. Nucl. Sci.* **1994**, *41*, 752–754. [CrossRef]
70. Kapusta, M.; Pawelke, J.; Moszyński, M. Comparison of YAP and BGO for high-resolution PET detectors. *Nucl. Instrum. Methods Phys. Res. A* **1998**, *404*, 413–417. [CrossRef]
71. Schotanus, P.; Dorenbos, P.; Ryzhikov, V.D. Detection of CdS(Te) and ZnSe(Te) scintillation light with silicon photodiodes. *IEEE Trans. Nucl. Sci.* **1992**, *39*, 546–550. [CrossRef]
72. Raue, R.; Shiiki, M.; Matsukiyo, H.; Toyama, H.; Yamamoto, H. Saturation of ZnS:Ag and Al under cathode X-ray excitation. *J. Appl. Phys.* **1994**, *75*, 481–488. [CrossRef]
73. Hotta, S. *Electronic and Optical Properties of Conjugated Molecular Systems in Condensed Phases*; Research Signpost: Kerala, India, 2003.
74. Yanagida, T.; Watanabe, K.; Fujimoto, Y. Comparative study of neutron and gamma-ray pulse shape discrimination of anthracene, stilbene, and p-terphenyl. *Nucl. Instrum. Methods Phys. Res. A* **2015**, *784*, 111–114. [CrossRef]
75. Bass, C.; Beise, E.; Breuer, H.; Heimbach, C.; Langford, T.; Nico, J. Characterization of a ^{6}Li-loaded liquid organic scintillator for fast neutron spectrometry and thermal neutron detection. *Appl. Radiat. Isot.* **2013**, *77*, 130–138. [CrossRef] [PubMed]
76. Birks, J.B. Scintillations from Organic Crystals: Specific Fluorescence and Relative Response to Different Radiations. *Proc. Phys. Soc. Sect. A* **1951**, *64*, 874. [CrossRef]
77. Zaitseva, N.; Glenn, A.; Carman, L.; Martinez, H.P.; Hatarik, R.; Klapper, H.; Payne, S. Scintillation properties of solution-grown trans-stilbene single crystals. *Nucl. Instrum. Methods Phys. Res. A* **2015**, *789*, 8–15. [CrossRef]
78. Smeltzer, J.C. Energy Dependence of the Naphthalene Scintillation Detector. *Rev. Sci. Instrum.* **1950**, *21*, 669–669. [CrossRef] [PubMed]
79. Adrova, N.A.; Koton, M.M.; Florinsky, F.S. Preparation of 2,5-diphenyloxazole and its. scintillation efficiency in plastics. *Bull. Acad. Sci. USSR* **1957**, *6*, 394–395. [CrossRef]
80. Wegh, R.T.; Donker, H.; Oskam, K.D.; Meijerink, A. Visible Quantum Cutting in LiGdF^{4}:Eu^{3+} Through Downconversion. *Science* **1999**, *283*, 663–666. [CrossRef] [PubMed]
81. Yu, D.; Martín-Rodríguez, R.; Zhang, Q.; Meijerink, A.; Rabouw, F.T. Multi-photon quantum cutting in Gd_2O_2S:Tm^{3+} to enhance the photo-response of solar cells. *Light Sci. Appl.* **2015**, *4*, e344. [CrossRef]
82. Zych, E.; Meijerink, A.; de Mello Doneg, C. Quantum efficiency of europium emission from nanocrystalline powders of Lu2O3:Eu. *J. Phys. Condens. Matter* **2003**, *15*, 5145–5155. [CrossRef]
83. Birowosuto, M.D.; Dorenbos, P. Novel γ- and X-ray Scintillator Research: On the Emission Wavelength, Light Yield and Time Response of Ce^{3+} Doped Halide Scintillators. *Phys. Status Solidi A* **2009**, *206*, 9–20. [CrossRef]
84. Moszyński, M.; Wolski, D.; Ludziejewski, T.; Kapusta, M.; Lempicki, A.; Brecher, C.; Wiśniewski, D.; Wojtowicz, A. Properties of the new LuAP:Ce scintillator. *Nucl. Instrum. Methods Phys. Res. A* **1997**, *385*, 123–131. [CrossRef]
85. Drozdowski, W.; Wojtowicz, A.J.; Lukasiewicz, T.; Kisielewski, J. Scintillation properties of LuAP and LuYAP crystals activated with Cerium and Molybdenum. *Nucl. Instrum. Methods Phys. Res. A* **2006**, *562*, 254–261. [CrossRef]
86. Alekhin, M.S.; de Haas, J.T.M.; Khodyuk, I.V.; Kramer, K.W.; Menge, P.R.; Ouspenski, V.; Dorenbos, P. Improvement of γ-ray energy resolution of $LaBr_3$:Ce^{3+} scintillation detectors by Sr^{2+} and Ca^{2+} co-doping. *Appl. Phys. Lett.* **2013**, *102*, 161915. [CrossRef]
87. Bessiere, A.; Dorenbos, P.; van Eijk, C.; Krämer, K.; Güdel, H.; de Mello Donega, C.; Meijerink, A. Luminescence and scintillation properties of the small bandgap compound LaI_3:Ce^{3+}. *Nucl. Instrum. Methods Phys. Res. A* **2005**, *537*, 22–26. [CrossRef]
88. Birowosuto, M.D.; Dorenbos, P.; de Haas, J.T.M.; van Eijk, C.W.E.; Krämer, K.W.; Güdel, H.U. Optical Spectroscopy and Luminescence Quenching of LuI_3:Ce^{3+}. *J. Lumin.* **2006**, *118*, 308–316. [CrossRef]
89. Birowosuto, M.D.; Dorenbos, P.; van Eijk, C.W.E.; Krämer, K.W.; Güdel, H.U. High-light-output scintillator for photodiode readout: LuI_3:Ce^{3+}. *J. Appl. Phys.* **2006**, *99*, 123520. [CrossRef]
90. Birowosuto, M.D.; Dorenbos, P.; van Eijk, C.W.E.; Krämer, K.W.; Güdel, H.U. Scintillation properties of LuI_3:Ce^{3+}-high–light yield scintillators. *IEEE Trans. Nucl. Sci.* **2005**, *52*, 1114–1118. [CrossRef]
91. C Watson, C.; Casey, M.; Eriksson, L.; Mulnix, T.; Adams, D.; Bendriem, B. NEMA NU 2 performance tests for scanners with intrinsic radioactivity. *J. Nucl. Med.* **2004**, *45*, 822–6.

92. Moses, W.; Derenzo, S. The scintillation properties of cerium-doped lanthanum fluoride. *Nucl. Instrum. Methods Phys. Res. A* **1990**, *299*, 51 –56. [CrossRef]
93. Schotanus, P.; Eijk, C.V.; Hollander, R. Detection of LaF_3:Nd^{3+} scintillation light in a photosensitive multiwire chamber. *Nucl. Instrum. Methods Phys. Res. A* **1988**, *272*, 913 –916. [CrossRef]
94. Dorenbos, P.; Visser, R.; van Eijk, C.W.E.; Khaidukov, N.M.; Korzhik, M.V. Scintillation properties of some Ce^{3+} and Pr^{3+} doped inorganic crystals. *IEEE Trans. Nucl. Sci.* **1993**, *40*, 388–394. [CrossRef]
95. van Loef, E.V.D.; Dorenbos, P.; van Eijk, C.W.E.; Krämer, K.; Güdel, H.U. High-energy-resolution scintillator:Ce^{3+} activated $LaCl_3$. *Appl. Phys. Lett.* **2000**, *77*, 1467–1468. [CrossRef]
96. Birowosuto, M.D.; Dorenbos, P.; van Eijk, C.W.E.; Krämer, K.W.; Güdel, H.U. Thermal Quenching of Ce^{3+} Emission in PrX_3 (X = Cl, Br) by Intervalence Charge Transfer. *J. Phys. Condens. Matter* **2007**, *19*, 256209. [CrossRef]
97. van Loef, E.V.D.; Dorenbos, L.P.; van Eijk, C.W.E.; Kramer, K.; Gudel, H.U. Scintillation properties of $LaCl_3$:Ce^{3+} crystals: fast, efficient, and high-energy resolution scintillators. *IEEE Trans. Nucl. Sci.* **2001**, *48*, 341–345. [CrossRef]
98. Glodo, J.; van Loef, E.; Hawrami, R.; Higgins, W.M.; Churilov, A.; Shirwadkar, U.; Shah, K.S. Selected Properties of Cs_2LiYCl_6, $Cs_2LiLaCl_6$, and $Cs_2LiLaBr_6$ Scintillators. *IEEE Trans. Nucl. Sci.* **2011**, *58*, 333–338. [CrossRef]
99. Bessiere, A.; Dorenbos, P.; van Eijk, C.W.E.; Kramer, K.W.; Gudel, H.U. New thermal neutron scintillators: Cs_2LiYCl_6:Ce^{3+} and Cs_2LiYBr_6:Ce^{3+}. *IEEE Trans. Nucl. Sci.* **2004**, *51*, 2970–2972. [CrossRef]
100. van Loef, E.V.D.; Glodo, J.; Higgins, W.M.; Shah, K.S. Optical and scintillation properties of Cs_2LiYCl_6:Ce^{3+} and Cs_2LiYCl_6:Pr^{3+} crystals. *IEEE Trans. Nucl. Sci.* **2005**, *52*, 1819–1822. [CrossRef]
101. van 't Spijker, J.; Dorenbos, P.; van Eijk, C.; Krämer, K.; Güdel, H. Scintillation and luminescence properties of Ce^{3+} doped K_2LaCl_5. *J. Lumin.* **1999**, *85*, 1–10. [CrossRef]
102. van't Spijker, J.; Frijns, O.W.V.; Dorenbos, P.; van Eijk, C.; Krämer, K.; Güdel, H. $RbGd_2Cl_7$:Ce^{3+} and $RbGd_2Br_7$: Ce^{3+}: New Scintillators with a High Light Yield. In Proceedings of the International Conference on Inorganic Scintillators and their Applications, Shanghai, China, 22–25 September 1997; Yin, Z., Ed.; Crystal Clear Collaboration, Chinese Academy of Sciences: Shanghai, China, 1997; Volume 2, p. 330.
103. van Loef, E.V.D.; Dorenbos, P.; van Eijk, C.W.E.; Krämer, K.; Güdel, H.U. High-energy-resolution scintillator:Ce^{3+} activated $LaBr_3$. *Appl. Phys. Lett.* **2001**, *79*, 1573–1575. [CrossRef]
104. Glodo, J.; Farrell, R.; van Loef, E.V.D.; Higgins, W.M.; Shah, K.S. $LaBr_3$:Pr^{3+}—A new red-emitting scintillator. *IEEE Nucl. Sci. Symp. Conf. Rec.* **2005**, *1*, 98–101.
105. van Loef, E.; Dorenbos, P.; van Eijk, C.; Krämer, K.; Güdel, H. Optical and scintillation properties of pure and Ce^{3+} doped $GdBr_3$. *Opt. Comm.* **2001**, *189*, 297–304. [CrossRef]
106. Birowosuto, M.D.; Dorenbos, P.; van Eijk, C.W.E.; Krämer, K.W.; Güdel, H.U. Scintillation and luminescence properties of Ce^{3+} doped ternary cesium rare-earth halides. *Phys. Stat. Sol. A* **2007**, *204*, 850–860. [CrossRef]
107. Birowosuto, M.D.; Dorenbos, P.; van Eijk, C.W.E.; Krämer, K.W.; Güdel, H.U. Scintillation properties and anomalous Ce^{3+} emission of $Cs_2NaREBr_6$:Ce^{3+} (RE = La, Y, Lu). *J. Phys. Condens. Matter* **2006**, *18*, 6133–6148. [CrossRef] [PubMed]
108. van Loef, E.; Dorenbos, P.; van Eijk, C.; Krämer, K.; Güdel, H. Scintillation properties of K_2LaX_5:Ce^{3+} (X = Cl, Br, I). *Nucl. Instrum. Methods Phys. Res. A* **2005**, *537*, 232 –236. [CrossRef]
109. Birowosuto, M.D.; Dorenbos, P.; Haas, J.T.M.D.; Eijk, C.W.E.V.; Krämer, K.W.; Güdel, H.U. Li-Based Thermal Neutron Scintillator Research; Rb_2LiYBr_6:Ce^{3+} and Other Elpasolites. *IEEE Trans. Nucl. Sci.* **2008**, *55*, 1152–1155. [CrossRef]
110. Birowosuto, M.D.; Dorenbos, P.; Bizarri, G.; van Eijk, C.W.E.; Kraemer, K.W.; Guedel, H.U. Temperature dependent scintillation and luminescence characteristics of GdI_3: Ce^{3+}. *IEEE Trans. Nucl. Sci.* **2008**, *55*, 1164–1169. [CrossRef]
111. Grabmeier, B.C.; Rossner, W.; Berthold, T. Phospors in X-ray Computed Tomography and for the gamma-ray Anger Camera. In Proceedings of the International Conference on Inorganic Scintillators and Their Applications, Delft, The Netherlands, 28 August–September 1 1995; van Eijk, C.W.E., Ed.; Crystal Clear Collaboration, Delft University of Technology: Delft, The Nertherlands, 1995; Volume 1, p. 29.
112. Moszyński, M.; Kapusta, M.; Wolski, D.; Klamra, W.; Cederwall, B. Properties of the YAP: Ce scintillator. *Nucl. Instrum. Methods Phys. Res. A* **1998**, *404*, 157–165. [CrossRef]

113. Mihóková, E.; Nikl, M.; Mareš, J.; Beitlerová, A.; Vedda, A.; Nejezchleb, K.; Blažek, K.; D'Ambrosio, C. Luminescence and scintillation properties of YAG:Ce single crystal and optical ceramics. *J. Lumin.* **2007**, *126*, 77–80. [CrossRef]
114. Ogino, H.; Yoshikawa, A.; Nikl, M.; Krasnikov, A.; Kamada, K.; Fukuda, T. Growth and scintillation properties of Pr-doped $Lu_3Al_5O_{12}$ crystals. *J. Crys. Growth* **2006**, *287*, 335–338. [CrossRef]
115. Nikl, M.; Yoshikawa, A.; Vedda, A.; Fukuda, T. Development of novel scintillator crystals. *J. Cryst. Growth* **2006**, *292*, 416–421. [CrossRef]
116. Pauwels, D.; Masson, N.L.; Viana, B.; Kahn-Harari, A.; van Loef, E.V.D.; Dorenbos, P.; van Eijk, C.W.E. A novel inorganic scintillator: $Lu_2Si_2O_7$:Ce^{3+} (LPS). *IEEE Trans. Nucl. Sci.* **2000**, *47*, 1787–1790. [CrossRef]
117. Drozdowski, W.; Brylew, K.; Wojtowicz, A.J.; Kisielewski, J.; Świrkowicz, M.; Łukasiewicz, T.; de Haas, J.T.; Dorenbos, P. 33000 photons per MeV from mixed $(Lu_{0.75}Y_{0.25})_3Al_5O_{12}$:Pr scintillator crystals. *Opt. Mater. Express* **2014**, *4*, 1207–1212. [CrossRef]
118. Mareš, J.A.; Jacquier, B.; Pédrini, C.; Boulon, G. Fluorescence decays and lifetimes of Nd^{3+}, Ce^{3+} and Cr^{3+} in YAG. *Czech. J. Phys. B* **1988**, *38*, 802–816. [CrossRef]
119. Drozdowski, W.; Dorenbos, P.; de Haas, J.T.M.; Drozdowska, R.; Owens, A.; Kamada, K.; Tsutsumi, K.; Usuki, Y.; Yanagida, T.; Yoshikawa, A. Scintillation Properties of Praseodymium Activated $Lu_3Al_5O_{12}$ Single Crystals. *IEEE Trans. Nucl. Sci.* **2008**, *55*, 2420–2424. [CrossRef]
120. Melcher, C.L.; Schweitzer, J.S.; Peterson, C.A.; Manente, R.A.; Suzuki, H. Crystal growth and scintillation properties of the rare earth orthosilicates. In Proceedings of the International Conference on Inorganic Scintillators and Their Applications, Delft, The Netherlands, 28 August–1 September 1996; van Eijk, C.W.E., Ed.; Crystal Clear Collaboration, Delft University of Technology: Delft, The Netherlands, 1995; Volume 1, p. 309.
121. Kawamura, S.; Kaneko, J.H.; Higuchi, M.; Yamaguchi, T.; Haruna, J.; Yagi, Y.; Susa, K.; Fujita, F.; Homma, A.; Nishiyama, S.; et al. Floating Zone Growth and Scintillation Characteristics of Cerium-Doped Gadolinium Pyrosilicate Single Crystals. *IEEE Trans. Nucl. Sci.* **2007**, *54*, 1383–1386. [CrossRef]
122. Shimizu, S.; Kurashige, K.; Usui, T.; Shimura, N.; Sumiya, K.; Senguttuvan, N.; Gunji, A.; Kamada, M.; Ishibashi, H. Scintillation properties of $Lu_{0.4}Gd_{1.6}SiO_5$: Ce (LGSO) crystal. *IEEE Trans. Nucl. Sci.* **2006**, *53*, 14–17. [CrossRef]
123. Selling, J.; Birowosuto, M.D.; Dorenbos, P.; Schweizer, S. Europium-doped barium halide scintillators for X-ray and gamma-ray detections. *J. Appl. Phys.* **2007**, *101*, 034901. [CrossRef]
124. Cherepy, N.J.; Hull, G.; Niedermayr, T.R.; Drobshoff, A.; Payne, S.A.; Roy, U.N.; Cui, Y.; Bhattacharaya, A.; Harrison, M.; Guo, M.; et al. Barium iodide single-crystal scintillator detectors. *Proc. SPIE* **2007**, *6706*.
125. Gundiah, G.; Bourret-Courchesne, E.; Bizarri, G.; Hanrahan, S.M.; Chaudhry, A.; Canning, A.; Moses, W.W.; Derenzo, S.E. Scintillation properties of Eu^{2+}-activated barium fluoroiodide. *IEEE Trans. Nucl. Sci.* **2010**, *57*, 3. [CrossRef]
126. Gundiah, G.; Yan, Z.; Bizarri, G.; Derenzo, S.E.; Bourret-Courchesne, E.D. Structure and scintillation of Eu^{2+}-activated BaBrCl and solid solutions in the $BaCl_2$–$BaBr_2$ system. *J. Lumin.* **2013**, *138*, 143–149. [CrossRef]
127. Bourret-Courchesne, E.; Bizarri, G.; Borade, R.; Gundiah, G.; Samulon, E.; Yan, Z.; Derenzo, S. Crystal growth and characterization of alkali-earth halide scintillators. *J. Crys. Growth* **2012**, *352*, 78–83. [CrossRef]
128. Bizarri, G.; Bourret-Courchesne, E.D.; Yan, Z.; Derenzo, S.E. Scintillation and Optical Properties BaBrI:Eu^{2+} and $CsBa_2I_5$:Eu^{2+}. *IEEE Trans. Nucl. Sci.* **2011**, *58*, 3403–3410. [CrossRef]
129. Derenzo, S.; Bizarri, G.; Borade, R.; Bourret-Courchesne, E.; Boutchko, R.; Canning, A.; Chaudhry, A.; Eagleman, Y.; Gundiah, G.; Hanrahan, S.; et al. New scintillators discovered by high-throughput screening. *Nucl. Instrum. Methods Phys. Res. A* **2011**, *652*, 247–250. [CrossRef]
130. Holl, I.; Lorenz, E.; Mageras, G. A measurement of the light yield of common inorganic scintillators. *IEEE Trans. Nucl. Sci.* **1988**, *35*, 105–109. [CrossRef]
131. Grippa, A.; Rebrova, N.; Gorbacheva, T.; Pedash, V.; Kosinov, N.; Cherginets, V.; Tarasov, V.; Tarasenko, O.; Lopin, A. Scintillation properties of $CaBr_2$ crystals doped with Eu^{2+} ions. *Nucl. Instrum. Methods Phys. Res. A* **2013**, *729*, 356–359. [CrossRef]
132. Cherepy, N.J.; Payne, S.A.; Asztalos, S.J.; Hull, G.; Kuntz, J.D.; Niedermayr, T.; Pimputkar, S.; Roberts, J.J.; Sanner, R.D.; Tillotson, T.M.; et al. Scintillators With Potential to Supersede Lanthanum Bromide. *IEEE Trans. Nucl. Sci.* **2009**, *56*, 873–880. [CrossRef]
133. Borade, R.; Bourret-Courchesne, E.; Derenzo, S. Scintillation properties of $CsBa_2Br_5$:Eu^{2+}. *Nucl. Instrum. Methods Phys. Res. A* **2011**, *652*, 260–263. [CrossRef]

134. Rowe, E.; Bhattacharya, P.; Tupitsyn, E.; Groza, M.; Burger, A.; Cherepy, N.J.; Payne, S.A.; Sturm, B.W.; Pédrini, C. A New Lanthanide Activator for Iodide Based Scintillators:Yb^{2+}. *IEEE Trans. Nucl. Sci.* **2013**, *60*, 1057–1060. [CrossRef]
135. Zhuravleva, M.; Blalock, B.; Yang, K.; Koschan, M.; Melcher, C.L. New single crystal scintillators: $CsCaCl_3$:Eu and $CsCaI_3$:Eu. *J. Cryst. Growth* **2012**, *352*, 115–119. [CrossRef]
136. Grippa, A.; Rebrova, N.; Gorbacheva, T.; Pedash, V.; Kosinov, N.; Cherginets, V.; Tarasov, V.; Tarasenko, O.; Lopin, A. Crystal growth and scintillation properties of $CsCaBr_3:Eu^{2+}$. *J. Cryst. Growth* **2013**, *371*, 112–116. [CrossRef]
137. Cherginets, V.; Rebrova, N.; Grippa, A.; Datsko, Y.; Ponomarenko, T.; Pedash, V.; Kosinov, N.; Tarasov, V.; Zelenskaya, O.; Zenya, I.; et al. Scintillation properties of $CsSrX_3:Eu^{2+}$ (X = Cl, Br) single crystals grown by the Bridgman method. *Mater. Chem. Phys.* **2014**, *143*, 1296–1299. [CrossRef]
138. Yang, K.; Zhuravleva, M.; Melcher, C.L. Crystal growth and characterization of $CsSrI_3:Eu^{2+}$ high–light yield scintillators. *Phys. Stat. Sol.* **2011**, *5*, 43–45.
139. Stand, L.; Zhuravleva, M.; Chakoumakos, B.; Johnson, J.; Lindsey, A.; Melcher, C. Scintillation properties of Eu^{2+}-doped KBa_2I_5 and K_2BaI_4. *J. Lumin.* **2016**, *169*, 301–307. [CrossRef]
140. Cherepy, N.J.; Hull, G.; Drobshoff, A.D.; Payne, S.A.; Van Loef, E.; Wilson, C.M.; Shah, K.S.; Roy, U.N.; Burger, A.; Boatner, L.A.; et al. Strontium and barium iodide high–light yield scintillators. *Appl. Phys. Lett.* **2008**, *92*, 90–93. [CrossRef]
141. Xie, A.; Nguyen, T.H.; Hettiarachchi, C.; Witkowski, M.E.; Drozdowski, W.; Birowosuto, M.D.; Wang, H.; Dang, C. Thermal Quenching and Dose Studies of X-ray Luminescence in Single Crystals of Halide Perovskites. *J. Phys. Chem. C* **2018**, *122*, 16265–16273. [CrossRef]
142. Wei, H.; Fang, Y.; Mulligan, P.; Chuirazzi, W.; Fang, H.H.; Wang, C.; Ecker, B.R.; Gao, Y.; Loi, M.A.; Cao, L.; et al. Sensitive X-ray Detectors Made of Methylammonium Lead Tribromide Perovskite Single Crystals. *Nat. Photon.* **2016**, *10*, 333–339. [CrossRef]
143. Kim, Y.C.; Kim, K.H.; Son, D.Y.; Jeong, D.N.; Seo, J.Y.; Choi, Y.S.; Han, I.T.; Lee, S.Y.; Park, N.G. Printable organometallic perovskite enables large-area, low-dose X-ray imaging. *Nature* **2017**, *550*, 87. [CrossRef] [PubMed]
144. Wei, W.; Zhang, Y.; Xu, Q.; Wei, H.; Fang, Y.; Wang, Q.; Deng, Y.; Li, T.; Gruverman, A.; Cao, L.; et al. Monolithic integration of hybrid perovskite single crystals with heterogenous substrate for highly sensitive X-ray imaging. *Nat. Photon.* **2017**, *11*, 315. [CrossRef]
145. Yakunin, S.; Sytnyk, M.; Kriegner, D.; Shrestha, S.; Richter, M.; Matt, G.J.; Azimi, H.; Brabec, C.J.; Stangl, J.; Kovalenko, M.V.; et al. Detection of X-ray photons by solution-processed lead halide perovskites. *Nat. Photon.* **2015**, *9*, 444–450. [CrossRef]
146. Shrestha, S.; Fischer, R.; Matt, G.J.; Feldner, P.; Michel, T.; Osvet, A.; Levchuk, I.; Merle, B.; Golkar, S.; Chen, H.; et al. High-Performance Direct Conversion X-ray Detectors Based on Sintered Hybrid Lead Triiodide Perovskite Wafers. *Nat. Photon.* **2017**, *11*, 436–440. [CrossRef]
147. Wei, H.; DeSantis, D.; Wei, W.; Deng, Y.; Guo, D.; Savenije, T.J.; Cao, L.; Huang, J. Dopant compensation in alloyed $CH_3NH_3PbBr_3$-xClx perovskite single crystals for gamma-ray spectroscopy. *Nat. Mater.* **2017**, *16*, 826. [CrossRef]
148. Tan, Z.K.; Moghaddam, R.S.; Lai, M.L.; Docampo, P.; Higler, R.; Deschler, F.; Price, M.; Sadhanala, A.; Pazos, L.M.; Credgington, D.; et al. Bright light-emitting diodes based on organometal halide perovskite. *Nat. Nanotechnol.* **2014**, *9*, 687–692. [CrossRef] [PubMed]
149. Chin, X.Y.; Perumal, A.; Bruno, A.; Yantara, N.; Veldhuis, S.A.; Martínez-Sarti, L.; Chandran, B.; Chirvony, V.; Lo, A.S.Z.; So, J.; et al. Self-assembled hierarchical nanostructured perovskites enable highly efficient LEDs via an energy cascade. *Energy Environ. Sci.* **2018**, *11*, 1770–1778. [CrossRef]
150. Shibuya, K.; Koshimizu, M.; Takeoka, Y.; Asai, K. Scintillation Properties of $(C_6H_{13}NH_3)_2PbI_4$: Exciton Luminescence of an Organic/Inorganic Multiple Quantum Well Structure Compound Induced by 2.0 MeV protons. *Nucl. Instrum. Methods Phys. Res. B* **2002**, *194*, 207–212. [CrossRef]
151. Kishimoto, S.; Shibuya, K.; Nishikido, F.; Koshimizu, M.; Haruki, R.; Yoda, Y. Subnanosecond time-resolved X-ray measurements using an organic-inorganic perovskite scintillator. *Appl. Phys. Lett.* **2008**, *93*, 261901. [CrossRef]
152. Ma, D.; Fu, Y.; Dang, L.; Zhai, J.; Guzei, I.A.; Jin, S. Single-crystal microplates of two-dimensional organic–inorganic lead halide layered perovskites for optoelectronics. *Nano Res.* **2017**, *10*, 2117–2129. [CrossRef]

153. Kawano, N.; Koshimizu, M.; Okada, G.; Fujimoto, Y.; Kawaguchi, N.; Yanagida, T.; Asai, K. Scintillating Organic-Inorganic Layered Perovskite-Type Compounds and the Gamma-Ray Detection Capabilities. *Sci. Rep.* **2017**, *7*, 14754. [CrossRef] [PubMed]
154. Eperon, G.E.; Paternò, G.M.; Sutton, R.J.; Zampetti, A.; Haghighirad, A.A.; Cacialli, F.; Snaith, H.J. Inorganic caesium lead iodide perovskite solar cells. *J. Mater. Chem. A* **2015**, *3*, 19688–19695. [CrossRef]
155. Diguna, L.J.; Tjahjana, L.; Darma, Y.; Zeng, S.; Wang, H.; Birowosuto, M.D. Light and Matter Interaction of Single Quantum Emitters with Dielectric Nanostructures. *Photonics* **2018**, *5*, 14. [CrossRef]
156. Knapitsch, A.; Lecoq, P. Review on photonic crystal coatings for scintillators. *Int. J. Mod. Phys. A* **2014**, *29*, 1430070. [CrossRef]
157. Salomoni, M.; Pots, R.; Auffray, E.; Lecoq, P. Enhancing Light Extraction of Inorganic Scintillators Using Photonic Crystals. *Crystals* **2018**, *8*, 78. [CrossRef]
158. Liu, J.; Liu, B.; Zhu, Z.; Chen, L.; Hu, J.; Xu, M.; Cheng, C.; Ouyang, X.; Zhang, Z.; Ruan, J.; et al. Modified timing characteristic of a scintillation detection system with photonic crystal structures. *Opt. Lett.* **2017**, *42*, 987–990. [CrossRef] [PubMed]
159. Knapitsch, A.; Auffray, E.; Fabjan, C.W.; Leclercq, J.; Letartre, X.; Mazurczyk, R.; Lecoq, P. Results of Photonic Crystal Enhanced Light Extraction on Heavy Inorganic Scintillators. *IEEE Trans. Nucl. Sci.* **2012**, *59*, 2334–2339. [CrossRef]
160. Hou, S.; Xie, A.; Xie, Z.; Tobing, L.Y.M.; Zhou, J.; Tjahjana, L.; Yu, J.; Hettiarachichi, C.; Zhang, D.; Dang, C.; et al. Concurrent Inhibition and Redistribution of Spontaneous Emission from All Inorganic Perovskite Photonic Crystals. **2018**, in submission.
161. Zhu, Z.; Wu, S.; Xue, C.; Zhao, J.; Wang, L.; Wu, Y.; Liu, B.; Cheng, C. Enhanced light extraction of scintillator using large-area photonic crystal structures fabricated by soft-X-ray interference lithography. *Appl. Phys. Lett.* **2015**, *106*, 241901. [CrossRef]
162. Pourdavoud, N.; Wang, S.; Mayer, A.; Hu, T.; Chen, Y.; Marianovich, A.; Kowalsky, W.; Heiderhoff, R.; Scheer, H.C.; Riedl, T. Photonic Nanostructures Patterned by Thermal Nanoimprint Directly into Organo-Metal Halide Perovskites. *Adv. Mater.* **2017**, *29*, 1605003. [CrossRef]
163. Gholipour, B.; Adamo, G.; Cortecchia, D.; Krishnamoorthy, H.N.S.; Birowosuto, M.D.; Zheludev, N.I.; Soci, C. Organometallic Perovskite Metasurfaces. *Adv. Mater.* **2017**, *29*, 1604268. [CrossRef]
164. Bulin, A.L.; Vasil'ev, A.; Belsky, A.; Amans, D.; Ledoux, G.; Dujardin, C. Modelling energy deposition in nanoscintillators to predict the efficiency of the X-ray-induced photodynamic effect. *Nanoscale* **2015**, *7*, 5744–5751. [CrossRef] [PubMed]
165. Yaffe, M.J.; Rowlands, J.A. X-ray detectors for digital radiography. *Phys. Med. Biol.* **1997**, *42*, 1–39. [CrossRef]
166. Kang, Z.; Zhang, Y.; Menkara, H.; Wagner, B.K.; Summers, C.J.; Lawrence, W.; Nagarkar, V. CdTe quantum dots and polymer nanocomposites for X-ray scintillation and imaging. *Appl. Phys. Lett.* **2011**, *98*, 181914. [CrossRef] [PubMed]
167. Xu, G.; Zeng, S.; Zhang, B.; Swihart, M.T.; Yong, K.T.; Prasad, P.N. New Generation Cadmium-Free Quantum Dots for Biophotonics and Nanomedicine. *Chem. Rev.* **2016**, *116*, 12234–12327. [CrossRef] [PubMed]
168. Burke, E.R.; DeHaven, S.L.; Williams, P.A. Scintillating quantum dots for imaging X-rays (SQDIX) for aircraft inspection. *AIP Conf. Proc.* **2016**, *1706*, 110007.
169. Protesescu, L.; Yakunin, S.; Bodnarchuk, M.I.; Krieg, F.; Caputo, R.; Hendon, C.H.; Yang, R.X.; Walsh, A.; Kovalenko, M.V. Nanocrystals of Cesium Lead Halide Perovskites ($CsPbX_3$, X = Cl, Br, and I): Novel Optoelectronic Materials Showing Bright Emission with Wide Color Gamut. *Nano Lett.* **2015**, *15*, 3692–3696. [CrossRef] [PubMed]
170. Chen, Q.; Wu, J.; Ou, X.; Huang, B.; Almutlaq, J.; Zhumekenov, A.A.; Guan, X.; Han, S.; Liang, L.; Yi, Z.; et al. All-inorganic perovskite nanocrystal scintillators. *Nature* **2018**, *561*, 88–93. [CrossRef] [PubMed]
171. Heo, J.H.; Shin, D.H.; Park, J.K.; Kim, D.H.; Lee, S.J.; Im, S.H. High-Performance Next-Generation Perovskite Nanocrystal Scintillator for Nondestructive X-ray Imaging. *Adv. Mater.* **2018**, *30*, 1801743. [CrossRef] [PubMed]



© 2019 by the authors. Licensee MDPI, Basel, Switzerland. This article is an open access article distributed under the terms and conditions of the Creative Commons Attribution (CC BY) license (http://creativecommons.org/licenses/by/4.0/).